Predictability and Decadal Variability of the North Atlantic Ocean State Evaluated from a Realistic Ocean Model

FLORIAN SÉVELLEC

Ocean and Earth Science, University of Southampton, Southampton, United Kingdom

ALEXEY V. FEDOROV

Department of Geology and Geophysics, Yale University, New Haven, Connecticut

(Manuscript received 19 April 2016, in final form 12 September 2016)

ABSTRACT

This study investigates the excitation of decadal variability and predictability of the ocean climate state in the North Atlantic. Specifically, initial linear optimal perturbations (LOPs) in temperature and salinity that vary with depth, longitude, and latitude are computed, and the maximum impact on the ocean of these perturbations is evaluated in a realistic ocean general circulation model. The computations of the LOPs involve a maximization procedure based on Lagrange multipliers in a nonautonomous context. To assess the impact of these perturbations four different measures of the North Atlantic Ocean state are used: meridional volume and heat transports (MVT and MHT) and spatially averaged sea surface temperature (SST) and ocean heat content (OHC). It is shown that these metrics are dramatically different with regard to predictability. Whereas OHC and SST can be efficiently modified only by basin-scale anomalies, MVT and MHT are also strongly affected by smaller-scale perturbations. This suggests that instantaneous or even annual-mean values of MVT and MHT are less predictable than SST and OHC. Only when averaged over several decades do the former two metrics have predictability comparable to the latter two, which highlights the need for long-term observations of the Atlantic meridional overturning circulation in order to accumulate climatically relevant data. This study also suggests that initial errors in ocean temperature of a few millikelvins, encompassing both the upper and deep ocean, can lead to ~0.1-K errors in the predictions of North Atlantic sea surface temperature on interannual time scales. This transient error growth peaks for SST and OHC after about 6 and 10 years, respectively, implying a potential predictability barrier.

1. Introduction

Climate prediction on a range of time scales is progressing rapidly, with the ultimate goals extending from seasonal to decadal and centennial prediction (IPCC 2013). In the context of the ongoing climate change, it has been argued that on seasonal to decadal time scales uncertainty in climate prediction is related to the internal variability but on longer time scales (century) to the future scenario of CO_2 emissions (Hawkins and Sutton 2009b). Thus, the latter uncertainty is linked to societal choices, whereas the former is related to the adjustment of the climate system, which in numerical climate simulations depends, to a large extent, on the evolution of small errors in the initial conditions. In the present study we will focus on this particular uncertainty in decadal prediction, which presumably sets the limits on the predictability of the climate system at these time scales.

Despite notable improvements, our ability to predict climate for the next decade or so remains an open question in the scientific community, even though potentially it could have large societal implications. For example, predicting the Atlantic multidecadal oscillation/variability (Kushnir 1994; Delworth and Mann 2000) would be highly desirable as it influences hurricane activity (Goldenberg et al. 2001) and precipitation over North America and Europe (Sutton and Hodson 2005).

There are two main reasons why errors or offsets in the model initial conditions result in uncertainty. First,

Corresponding author address: Florian Sévellec, Ocean and Earth Science, University of Southampton, Waterfront campus, European Way, Southampton, SO14 3ZH, United Kingdom.
E-mail: florian.sevellec@noc.soton.ac.uk

DOI: 10.1175/JCLI-D-16-0323.1

they can induce a phase shift in the simulated climate variability. For instance, two identical, perfectly periodic oscillators initialized at different phases would evolve conserving their initial phase difference, leading to uncertainty. However, this uncertainty remains relatively constant in time and can be reduced, or even removed, by a good initial phasing of the climate system (i.e., by using more accurate initial conditions). Therefore, efforts have been directed to improve the accuracy of the initialization of numerical models used for climate prediction, and so to limit any phase shift in the simulations. This is done both by increasing the coverage and number of in situ measurements [e.g., the Array for Real-time Geostrophic Oceanography (ARGO) program], and by developing different state-estimate methods (e.g., variational assimilation; Weaver et al. 2003).

The second and perhaps more challenging problem is related to the growth of small errors in nonlinear systems such as climate. This concept, popularized as the "butterfly effect," follows the pioneering work of Lorenz (1963) on atmospheric dynamics. The error growth sets a theoretical limit on prediction, which for weather forecasting is estimated at about two weeks (Epstein 1988). For the climate system, wherein the short-term weather uncertainty averages out, this time scale remains largely unknown.

To address this problem, the scientific community has followed two main approaches. One approach involves ensemble experiments with slightly different initial conditions representing inherent errors in the model initialization. This pragmatic approach often concentrates on atmospheric errors, while the ocean is kept unperturbed initially. A more rigorous approach relies on computing small initial disturbances that can induce the maximum change in the system after a specified time, which is done by using generalized stability analysis (GSA; Farrell and Ioannou 1996a,b). Unlike linear stability analysis (Strogatz 1994), which only considers the system's asymptotic behavior, GSA accounts for transient phenomena, making it perfectly suitable for predictability studies. The main drawback of GSA against ensemble experiments is the assumption that the evolving perturbations remain small. Such an assumption, allowing the linearization of the system's equations around the climatological basic state, is valid for decadal variability of the Atlantic meridional overturning circulation (AMOC), which is typically weak compared to the mean AMOC intensity [e.g., 1 Sv vs 10 Sv in the IPSL-CM5 climate model ($1\,\mathrm{Sv} \equiv 10^6\,\mathrm{m^3\,s^{-1}}$); Mignot and Bony 2013], in particular during the Holocene period (Tziperman 1997).

Despite being less rigorous than GSA, studies using ensemble experiments have substantially improved our understanding of climate predictability. In an early paper, Griffies and Bryan (1997) suggested that the AMOC intensity had a predictability time scale on the order of 10–20 yr, whereas sea surface temperature was predictable at 5–7 yr. However, during intervals when multidecadal oscillatory variations were less prominent, predictability was strongly reduced because oceanic response to atmospheric noise dominated (Hasselmann 1976). More recently, Collins and Sinha (2003) argued that AMOC variations are potentially predictable one to two decades into the future, and this decadal predictability may lead to climate predictability for western Europe. This result, however, contradicts the study of Pohlmann et al. (2004), who suggest that although ocean surface temperatures over the North Atlantic (as well as the Southern Ocean) exhibit predictability on multidecadal time scales, surface air temperatures are only predictable over the ocean and maritime-influenced regions of Europe. Along the same lines, a series of studies suggest that AMOC variations, surface temperature, subsurface temperature, and upper ocean heat content are potentially predictable on decadal time scales (Collins et al. 2006; Msadek et al. 2010; Teng et al. 2011; Zanna 2012).

Overall, all these studies agree on a possible decadal predictability for the ocean; however, the quantitative details of this predictability remain contradictory. For example, whereas Persechino et al. (2013) suggest than the AMOC averaged over 5 to 10 years has a higher predictability than ocean heat content, Branstator and Teng (2014) argue that in the far north, Atlantic Ocean surface temperatures have predictability higher than that of the AMOC (up to 2 decades vs 8 years, respectively). Note that some of these studies use either experiments with a small number of ensemble members or truncated principal component analyses, known to underestimate error growth (Farrell and Ioannou 2001).

In recent years the use of GSA in the context of ocean circulation and climate dynamics on decadal time scales has seen an increase in popularity (e.g., Tziperman and Ioannou 2002; Zanna and Tziperman 2005; Sévellec et al. 2007; Tziperman et al. 2008; Zanna and Tziperman 2008; Sévellec et al. 2008; Hawkins and Sutton 2009a; Sévellec et al. 2009; Hawkins and Sutton 2011; Zanna et al. 2011; Sévellec and Fedorov 2015). In these studies two different methods are typically used: singular value decomposition (SVD; e.g., Tziperman and Ioannou 2002) and linear optimal perturbation(s) [LOP(s); e.g., Sévellec et al. 2007]. Whereas both methods deal with the transient growth of small perturbations, they have subtle differences in the way predictability is defined and estimated. The SVD method uses standard tools of linear algebra and requires solving an eigenvalue problem. The LOP method is derived from a more pragmatic approach that relies on an optimization problem whose

solutions describe the maximum linear growth of a chosen climatic variable over a given time. Schematically, in the context of predictability, SVD yields error growth evaluated via a quadratic norm (Lorenz 1965), whereas LOPs yield the full error bar (the upper bound) on a chosen climatic variable (Taylor et al. 2012). LOPs can also incorporate different additional constraints imposed in the process of optimization. Note that the two methods are not mutually exclusive, and for further comparison we refer the readers to Sévellec et al. (2007). LOPs can be more efficiently computed since they are given by explicit solutions of the optimization problem (rather than solutions of an eigenvalues problem for SVD). Because of this efficiency and the physical significance of the full error bar for a practical estimation of predictability, here we use the LOP method.

There exists a long history of perturbation studies based on similar methodological principles as the LOP approach described here. Indeed, since the pioneering work of Lorenz (1965), singular vectors have been broadly used to estimate error growth. Lorenz's work has been followed by a long series of other studies, especially in the context of predictability in atmospheric sciences. To name a few relevant approaches, we could cite Lyapunov vectors (e.g., Yoden and Nomura 1993) and finite time normal modes (e.g., Frederiksen 2000) used in a linear framework, or bred vectors (e.g., Baehr and Piontek 2014) and conditional nonlinear optimal perturbations applicable in a nonlinear framework (e.g., Mu and Zhang 2006; Zu et al. 2016).

In the current study, we will compute and apply LOPs to diagnose the predictability of several major metrics of the ocean state in the North Atlantic. Hence, predictability is assessed here by estimating the upper bound of the impact on the system of small disturbances. We will show that this predictability strongly depends on the metric used to measure the ocean state. Sea surface temperature and ocean heat content are predictable up to 6 and 10 years, respectively, whereas instantaneous values of ocean meridional volume and heat transports appear to be unpredictable. The predictability of the latter two metrics is improved by applying decadal averaging to the metrics; thus, averaged meridional volume and heat transport might be predictable on decadal time scales. Note that the above numbers describe the worst-case scenario based on the upper bound of error growth. Whether in practical cases a particular metric can be predicted for longer lead times will depend on how strongly model initialization errors project on the optimal perturbations.

The structure of the paper is as follows. In section 2, the ocean model, configuration, and seasonal cycle are described. The results of the analysis are given in section 3. An idealized model is used in section 4 to confirm analytically and further rationalize the main findings of the study. In section 5, implications of the results for ocean predictability will be given. Finally, section 6 includes discussions, conclusions, and directions for future work.

2. The ocean model, configuration, and seasonal cycle

The ocean GCM we use in this study, as well as its tangent linear and adjoint versions, has been employed in several previous studies by the same authors. In particular, they studied ocean sensitivity to initial perturbations in surface temperature and salinity (Sévellec et al. 2010; Sévellec and Fedorov 2013a,b, 2015) and to constant-in-time surface buoyancy fluxes (Sévellec and Fedorov 2016). While the model and the seasonal cycle it generates have been described in those studies, in this section we reproduce these descriptions for completeness.

a. *The model configuration*

In this study we use the ocean general circulation model (GCM) OPA 8.2 (Océan Parallélisé; Madec et al. 1998) in its 2° global configuration (ORCA2; Madec and Imbard 1996). There are 31 levels in the vertical, with the layer thickness varying from 10 m at the surface to 500 m at depth. The rigid-lid approximation is used. The primitive equations are discretized using an Arakawa C grid and the z coordinates.

Although a number of models participating in the last IPCC report [the Fifth Assessment Report (AR5)] used a 0.25° resolution in the ocean, our study takes advantage of a model with a lower resolution of 2° (note that the IPSL climate model uses the OPA as its oceanic component with the same 2° resolution, IPSL-CM5; Marti et al. 2010). The main reason for having the relatively coarse resolution is to avoid the small-scale baroclinic instability existing in eddy-permitting or eddy-resolving models. Within the linear framework of this study, such instability would not saturate, and as we are interested in large-scale basin adjustment this would contaminate the solutions of our experiments.

The present model configuration uses the following parameterizations: convection is parameterized by an increase in vertical diffusion when ocean stratification becomes unstable; double diffusion is taken into account by two different terms for mixing temperature and salinity; eddy-induced velocities are described by the Gent and McWilliams (1990) expression; viscosity coefficients follow the turbulent closure scheme of Blanke and Delecluse (1993) and are functions of longitude, latitude, and depth; and diffusion for temperature and salinity acts along isopycnal and diapycnal coordinates (Redi 1982).

The linear and adjoint models are provided by the OPATAM code (OPA Tangent Adjoint Model; Weaver et al. 2003). The tangent linear model is a linearization of the OPA's primitive equations of motions with respect to the ocean seasonally varying basic state.

In the present study, we use either the flux boundary conditions (with surface heat and freshwater fluxes specified) or mixed boundary conditions (with an SST restoring term is used in addition to specified freshwater fluxes). The restoring coefficient for SST is set to $40\,\mathrm{W\,m^{-2}\,K^{-1}}$ and $27.7\,\mathrm{mm\,day^{-1}\,psu^{-1}}$ (following standard values; Madec et al. 1998). The time-mean ocean fluxes were computed by running the full nonlinear model forced with a combination of the prescribed climatological fluxes and restoring terms (restoring to the climatological seasonal cycle). This latter approach produces a realistic seasonal cycle used by the linear and adjoint models, while reducing the damping and allowing SST anomalies to develop more easily (Huck and Vallis 2001; Arzel et al. 2006; Sévellec et al. 2009); for details, see below.

Several additional approximations have been introduced for the tangent-linear and adjoint models: viscosity coefficients in the momentum equations, tracer diffusivities, and eddy-induced advection are calculated only for the basic ocean state, and further variations in those coefficients are neglected.

b. The model seasonal cycle

The seasonally varying basic state of the ocean, also referred to as the annual model "trajectory," is obtained by the direct integration of the OPA model subject to the climatological surface boundary forcing (varying with the annual cycle). In particular, we used the ECMWF heat fluxes averaged in the interval from 1979 to 1993, the ERS wind stress blended with the TAO data between 1993 and 1996, and an estimate of the climatological river runoff. In addition, we applied a surface temperature restoring to the Reynolds climatological values averaged from 1982 to 1989, together with a surface salinity restoring to the Levitus (1989) climatology (we emphasize that the restoring term can be switched off in the experiments with the linear and adjoint models). A mass restoring term to the Levitus climatological values of temperature and salinity was applied in the Red and Mediterranean Seas. Starting with the Levitus climatology as the initial conditions, the model produces a quasi-stationary annual cycle of the ocean basic state after 200 years of integration.

The Atlantic meridional overturning circulation in the full ocean GCM (Fig. 1) is characterized by a northward mass transport above the thermocline, a southward return flow below 1000–1500 m and extending to about 3000 m, and a recirculation cell 3000 m associated with the Antarctic Bottom Water. The maximum volume transport of the AMOC is around 14 Sv, which is slightly below but still within the error bars of the observations (e.g., 18 ± 5 Sv; Talley et al. 2003). The AMOC poleward heat transport reaches 0.8 PW at 25°N, whereas estimates from inverse calculations and hydrographic sections give 1.3 PW at 24°N (Ganachaud and Wunsch 2000).

As expected, the SST field develops a strong meridional gradient in the northern Atlantic (Fig. 1), especially across the North Atlantic Current (NAC); it also develops a salinity maximum at about 20°N. The barotropic streamfunction shows an intense subtropical gyre and a weaker subpolar gyre centered at about 60°N. The two gyres are separated by the Gulf Stream and the NAC. Overall, the full nonlinear model produces a realistic (seasonally varying) basic state of the ocean. Next, we will conduct a generalized stability analysis of this ocean state, focusing on the ocean response to three-dimensional initial perturbations in temperature and salinity.

3. Optimal initial perturbations

a. Mathematical approach

The goal of these calculations is to obtain initial thermohaline (temperature and salinity) perturbations that will induce the largest change in the North Atlantic Ocean state after a given time within a linear framework. Here, we apply and extend the methodology originally proposed by Sévellec et al. (2007) and Sévellec et al. (2008). The text below follows from the derivation of Sévellec and Fedorov (2015) with a numbers of modifications pertinent to the present study.

The prognostic equations of the full nonlinear model can be written as a general nonautonomous dynamical system:

$$d_t|\mathbf{U}\rangle = \mathcal{N}(|\mathbf{U}\rangle, t), \tag{1}$$

where $\mathcal{N}$ is a time-dependent nonlinear operator, $|\mathbf{U}\rangle$ is a state vector consisting of all prognostic variables, and t is time. The state vector comprises the three-dimensional fields of temperature, salinity, and meridional and zonal velocity, together with the two-dimensional field of barotropic streamfunction. Since we study a finite-dimensional vector space, we can also define a dual vector $\langle\mathbf{U}|$ through the Euclidian scalar product $\langle\mathbf{U}\,|\,\mathbf{U}\rangle$.

We decompose the state vector as $|\mathbf{U}\rangle = |\overline{\mathbf{U}}\rangle + |\mathbf{u}\rangle$, where $|\overline{\boldsymbol{U}}\rangle$ is the nonlinear annual trajectory (i.e., the climatological background state) and $|\mathbf{u}\rangle$ is a perturbation. The temporal evolution of the perturbation follows a linear equation:

$$d_t|\mathbf{u}\rangle = \mathbf{A}(t)|\mathbf{u}\rangle, \mathbf{A}(t) = \left.\frac{\partial\mathcal{N}}{\partial|\mathbf{U}\rangle}\right|_{|\overline{\mathbf{U}}\rangle}, \tag{2}$$

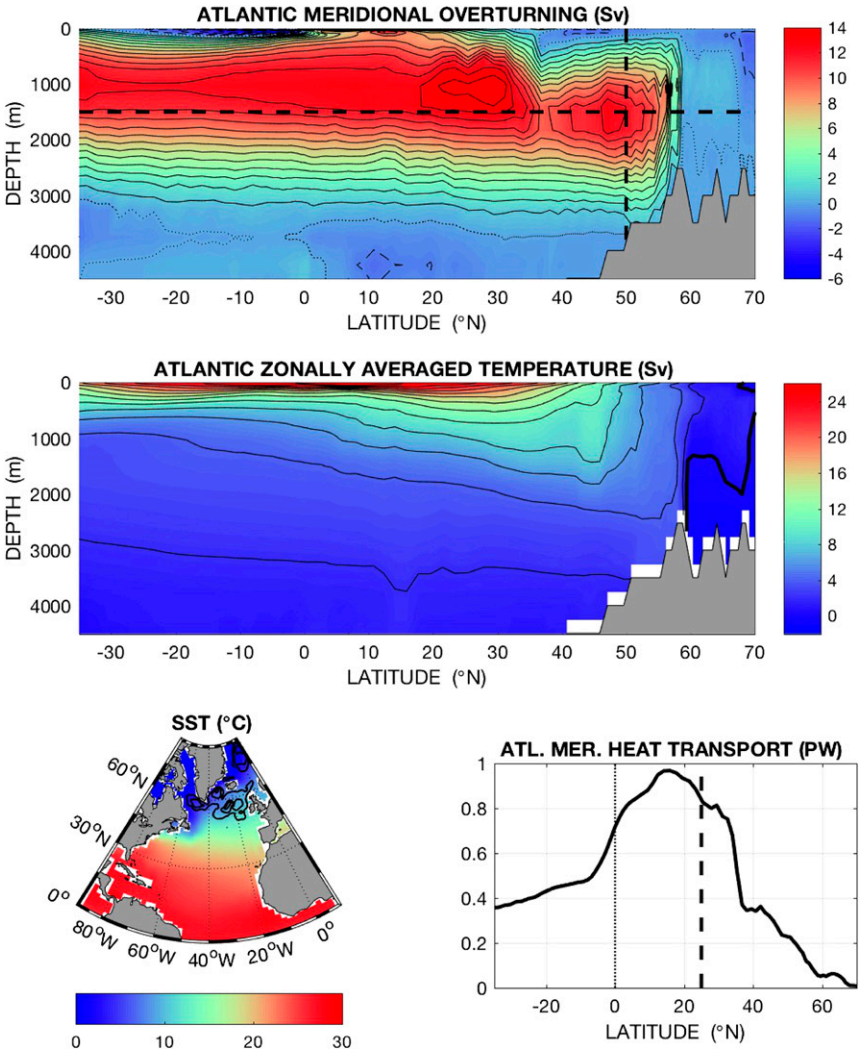

FIG. 1. The climatological basic state of the ocean in the Atlantic as reproduced by the full GCM. (top) Zonally averaged streamfunction of the Atlantic meridional overturning circulation; contour intervals (CI) are 1 Sv; plain, dashed, and dotted lines indicate positive, negative, and zero values. (middle) Zonally averaged temperature; CI are 2°C, the thick solid line corresponds to 0°C. (bottom left) SST (colors) and ocean mixed layer depth (contours); CI are 250 m. (bottom right) The Atlantic Ocean meridional heat transport as a function of latitude. In the top and bottom-right panels, the thick dashed horizontal and vertical lines indicate the latitudes and depth where MVT and MHT are estimated. These two variables along with spatially averaged OHC and SST in the North Atlantic are used as measures in the optimization problem. The figure is modified from Sévellec and Fedorov (2015).

where $\mathbf{A}(t)$ is a Jacobian matrix (a function of the trajectory $|\overline{\mathbf{U}}\rangle$). We also define an adjoint to the Jacobian matrix as $\langle \mathbf{a}|\mathbf{A}|\mathbf{b}\rangle = \langle \mathbf{b}|\mathbf{A}^{\dagger}|\mathbf{a}\rangle$, where $|\mathbf{a}\rangle$ and $|\mathbf{b}\rangle$ are two anomalous state vectors, and † denotes the adjoint defined through the Euclidian scalar product $\langle \mathbf{a}\,|\,\mathbf{b}\rangle = \langle \mathbf{b}\,|\,\mathbf{a}\rangle$.

After assuming that perturbations are and remain small, we can integrate (3.1) to obtain an explicit expression for the perturbation as a function of time (Farrell and Ioannou 1996b):

$$|\mathbf{u}(t_2)\rangle = \mathbf{M}(t_2, t_1)|\mathbf{u}(t_1)\rangle, \tag{3}$$

where $\mathbf{M}(t_2, t_1)$ is called the propagator of the linearized dynamics from time t_1 to time t_2. Following the study of Sévellec and Fedorov (2013a), using the exact same numerical model, we know that the propagator does not commute with its adjoint, that is, $\mathbf{M}^{\dagger}(t_2, t_1)\mathbf{M}(t_2, t_1) \neq \mathbf{M}(t_2, t_1)\mathbf{M}^{\dagger}(t_2, t_1)$. This defines the non-normality of the dynamics.

To evaluate the ocean state, we will compare four different measures (metrics) of the North Atlantic Ocean state:

1) meridional volume transport (MVT),
2) meridional heat transport (MHT),
3) spatially averaged sea surface temperature (SST), and
4) spatially averaged ocean heat content (OHC).

In general, the first two measures are nonlinear since the location of the measurements depends on the state of the system. However, they can still be used within the linear framework as long as MVT and MHT perturbations are evaluated at fixed locations where their climatological values are maximum (at $z_{\max(\overline{\mathrm{MVT}})} = 1500$ m deep and $y_{\max(\overline{\mathrm{MVT}})} = 50°$N for MVT and at $y_{\max(\overline{\mathrm{MHT}})} = 25°$N for MHT).

Thus, we can express anomalies in all of these four measures as linear functions of the state vector anomaly, $\langle \mathbf{F} \,|\, \mathbf{u} \rangle$, where $\langle \mathbf{F}|$ is an appropriate linear operator. Subsequently, $\langle \mathbf{F} \,|\, \mathbf{u} \rangle$ will be the cost function of the optimization procedure:

$$\langle F \,|\, \mathbf{u} \rangle = \begin{cases} \mathrm{MVT} = \displaystyle\int_{z_{\max(\overline{\mathrm{MVT}})}}^{0} \int_{x_W}^{x_E} v|_{y_{\max(\overline{\mathrm{MVT}})}} \, dx \, dz, \\ \mathrm{MHT} = \displaystyle\iint_{\Sigma} (\overline{v}T + v\overline{T})|_{y_{\max(\overline{\mathrm{MHT}})}} \, d\sigma, \\ \mathrm{SST} = \dfrac{1}{S_{\mathrm{NA}}} \displaystyle\iint_{\mathrm{NA}} T|_{z=0} \, ds, \\ \mathrm{OHC} = \dfrac{1}{V_{\mathrm{NA}}} \displaystyle\iiint_{\mathrm{NA}} T \, dv, \end{cases} \tag{4}$$

where $\overline{T}$ and T are the trajectory and anomalous temperature and v and $\overline{v}$ the trajectory and anomalous meridional component of velocity, respectively; x, y, and z are the zonal, meridional, and vertical coordinates, x_W and x_E are the specified zonal coordinates of the western and eastern basin boundaries, dv is a volume element, ds is a surface element of the ocean surface, $d\sigma$ is a surface element of a meridional section. S_{NA} is the total surface area of the North Atlantic, V_{NA} is the total volume of the North Atlantic basin, and Σ is the total area of a meridional section; NA indicates that the integral is restricted to the northern North Atlantic (i.e., from 30° to 70°N).

To analyze initial perturbations in temperature and salinity (rather than velocity), we need to reduce our parameter space. To that end, we define a projector $\mathbf{P}$ that connects the subspace of temperature and salinity to the full state vector as $|\mathbf{u}\rangle = \mathbf{P}|\mathbf{v}\rangle$, where $|\mathbf{v}\rangle$ represents a thermohaline vector. We also define two norms for these vectors in terms of their effect on density:

$$\begin{aligned} \langle \mathbf{u}|\mathbf{S}|\mathbf{u}\rangle &= \langle \mathbf{v}|\mathbf{P}^{\dagger}\mathbf{S}\mathbf{P}|\mathbf{v}\rangle = \langle \mathbf{v}|\mathbf{N}|\mathbf{v}\rangle \\ &= \frac{1}{V} \iiint (\alpha^2 T^2 + \beta^2 S^2) \, dv, \end{aligned} \tag{5}$$

where V is the ocean basin volume, T and S are temperature and salinity components of the full state vector, α is the thermal expansion coefficient, β is the haline contraction coefficient, $\mathbf{S}$ is a norm operator defined in the full state vector space, and $\mathbf{N}$ is the corresponding norm operator defined in the subspaces of temperature and salinity. These norms describe the model departure from the mean annual trajectory in terms of density (averaged over the basin).

Finally, we define a Lagrangian function as

$$\mathcal{L}(t_i, t_m) = \langle \mathbf{F} \,|\, \mathbf{u}(t_m) \rangle - \gamma [\langle \mathbf{u}(t_i)|\mathbf{S}|\mathbf{u}(t_i)\rangle - \epsilon^2], \tag{6}$$

where t_i is the initial time (when the optimal initial perturbation is applied), t_m is the maximization time (when the cost function reaches its maximum), and γ is a Lagrange multiplier. Also, ε is a parameter associated with the normalization constraint:

$$\langle \mathbf{u}(t_i)|\mathbf{S}|\mathbf{u}(t_i)\rangle = \epsilon^2. \tag{7}$$

That is, ε measures the magnitude of the initial perturbation (set to $\varepsilon/\alpha = 1$ mK). Thus, the goal here is to maximize the cost function subject to this normalization constraint.

From expression (6) and the optimization condition $d\mathcal{L} = 0$ the optimal initial perturbations are computed as

$$|\mathbf{u}^{\mathrm{opt}}_{\{t_i,t_m\}}(t_i)\rangle = \pm\epsilon \frac{\mathbf{P}\mathbf{N}^{-1}\mathbf{P}^{\dagger}\mathbf{M}^{\dagger}(t_i,t_m)|\mathbf{F}\rangle}{\sqrt{\langle \mathbf{F}|\mathbf{M}(t_m,t_i)\mathbf{P}\mathbf{N}^{-1}\mathbf{P}^{\dagger}\mathbf{M}^{\dagger}(t_i,t_m)|\mathbf{F}\rangle}}. \tag{8}$$

This expression gives a full explicit solution of the optimization problem, here referred to as the linear optimal perturbation. In general, LOPs depend both on the initial time t_i and the maximization time t_m. In this study we set t_m to the end of the year (31 December) and vary t_i. It turns out that the seasonal dependence of this solution is rather weak, which allows us to concentrate solely on decadal time scales. Consequently, we can define the time delay $\tau = t_i - t_m$ (<0) as one of the key parameters of the problem (which by definition of the LOP gives the duration of the transient growth in the system). Note that the seasonal cycle in the model is still important since it ensures an accurate representation of the mean state of the ocean.

To test the impacts of the model surface boundary conditions, two types of surface conditions are used to compute the LOPs: the mixed boundary conditions (MBC) and the flux boundary conditions (FBC). The

former apply surface temperature restoring and constant-in-time freshwater fluxes for salinity. The latter maintain constant surface heat and freshwater fluxes. MBC allow a feedback between oceanic and atmospheric temperatures, but assumes that the atmospheric heat reservoir is infinite. FBC neglect any feedbacks.

Realistic ocean–atmosphere interactions generate surface forcing for the ocean that lies probably somewhere in between these two extreme boundary conditions. Note that the annual trajectory remains identical for both set of experiments, and modifying surface boundary conditions affects only the tangent and adjoint simulations. We also remind the reader that using constant or even time-varying surface fluxes in the linearized problem means surface fluxes that are identically zero as long as the surface forcing is independent of ocean state variables.

As mentioned in the introduction, another common method to obtain optimal perturbations is based on the SVD (e.g., Farrell and Ioannou 1996a). Applying our approach (an optimization procedure using Lagrange multipliers) but maximizing a quadratic norm instead of a linear measure of the AMOC would lead to an eigenvalue problem whose solutions are singular vectors of the problem as shown in Sévellec et al. (2007). [A similar result has been independently obtained in the context of atmospheric modes of variability by Vimont (2010) and Martinez-Villalobos and Vimont (2016).] In the present and previous studies we choose to maximize linear measures for two main reasons. First, as discussed before, in a linear framework changes in MVT, MHT, SST, and OHC are conveniently expressed by linear functions of the state vector. Second, using linear measures yields an explicit solution of the problem, (8), which eliminates the necessity to solve an eigenvalue problem with much higher computational costs. A more extensive discussion of this point can be found in Sévellec et al. (2007).

b. Results

To check the existence of the most optimal (i.e., most effective) delay we have compared the impacts of the optimal perturbations of each measure in a range of τ from 0 to 1000 yr. Following (8), we have

$$\begin{aligned}\langle \mathbf{F} \,|\, \mathbf{u}_\tau^{\mathrm{opt}}(0)\rangle &= \langle \mathbf{F}|\mathbf{M}(-\tau)|\boldsymbol{u}_\tau^{\mathrm{opt}}(\tau)\rangle \\ &= \pm\epsilon\sqrt{\langle \mathbf{F}|\mathbf{M}(-\tau)\mathbf{P}\mathbf{N}^{-1}\mathbf{P}^\dagger\mathbf{M}^\dagger(\tau)|\mathbf{F}\rangle}\,. \end{aligned} \tag{9}$$

Using this diagnostic reveals striking differences in the system sensitivity of different measures (Fig. 2). Whereas OHC has an optimal transient time scale of one decade (more exactly −9.9 yr), MVT and MHT do not. The almost monotonically decreasing sensitivity of MVT and MHT to optimal initial perturbations as a function of time delay (Figs. 2a,b) suggests that MVT and MHT can be modified by nearly instantaneous perturbations (with just a few weeks or months delay) much more efficiently than by perturbations in the distant past. In contrast, OHC shows the highest sensitivity to perturbations applied a decade earlier (Fig. 2d).

Examining the SST sensitivity to optimal perturbations reveals two local maxima (Fig. 2c), one for zero

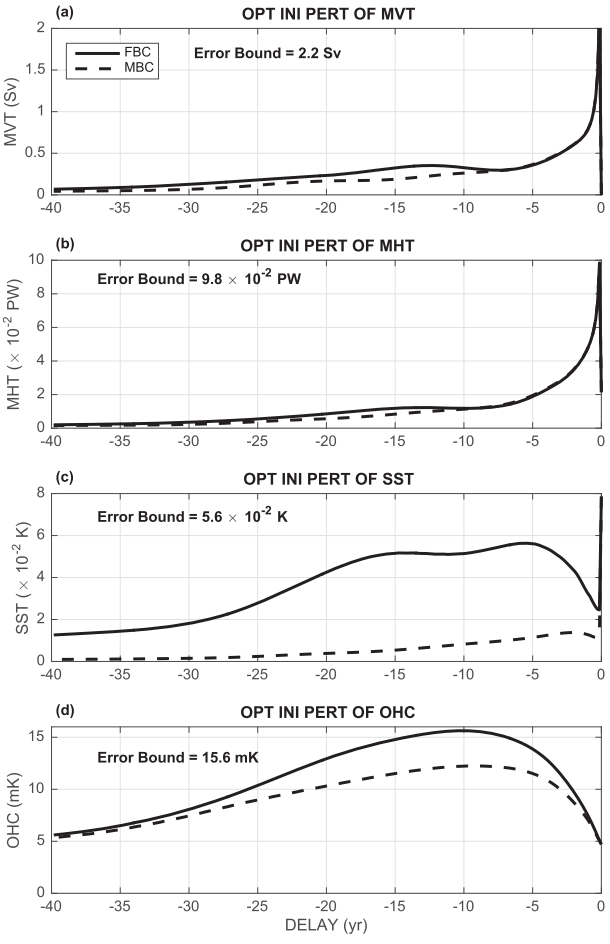

FIG. 2. (a)–(d) The impact of the optimal thermohaline perturbations of MVT, MHT, SST, and OHC on the respective variables as a function of the time delay τ. The impact is defined as the maximum magnitude that a particular variable would reach at the peak of the transient growth. Solid and dashed lines represent that MVT and MHT are affected most efficiently by near instantaneous perturbations ($\tau \simeq 0$), whereas OHC and SST are most sensitive to past perturbations. The choice of the boundary conditions is most important for SST. Hereafter, in Figs. 2–7 and 9–12, the magnitude of the initial perturbations given by the norm is scaled to the order of 1 mK (i.e., $\alpha^{-1}\sqrt{\langle \mathbf{u}(0)|\mathbf{S}|\mathbf{u}(0)\rangle} = 10^{-3}$ K). In the context of ocean predictability, the error bound is defined as the maximum impact of a particular initial perturbation with this magnitude across all tested delays for FBC (instantaneous values are disregarded for SST; see the text).

delay and another for a delay in the interannual range (−5.8 yr). The zero-delay maximum in sensitivity corresponds to the trivial result of a spatially uniform surface temperature anomaly in the North Atlantic with no subsurface signature. Such sensitivity disappears for delays longer than one month is disregarded here. Consequently, in the rest of this study we will consider only the ~6-yr maximum in the SST sensitivity.

For all four measures used, the impacts of initial perturbations are greater under fixed boundary conditions than under mixed boundary conditions as the surface temperature restoring limits the impact of surface temperature anomalies (solid vs dashed lines in Fig. 2). Indeed, since by construction LOPs avoid inefficient contributions, the temperature signature of LOPs for MBC is close to zero at the ocean surface, which weakens the overall impacts of optimal perturbations for this type of boundary conditions. The differences between FBC and MBC become more pronounced when the spatially averaged SST is used as the measure, because this particular variable is directly affected by the choice of surface boundary conditions for temperature (Fig. 2c). In contrast, for measures such as to MVT and MHT, the results corresponding to different boundary conditions start diverging only after one decade. This suggests that the impacts of initial perturbations (except for SST) are relatively insensitive to the choice of surface boundary conditions, especially since the maximum sensitivity emerges within the first decade.

Considering the spatial structure of the optimal initial perturbations with the most efficient delay reveals striking differences in the horizontal length scale of the perturbations, especially in the zonal direction. Whereas the optimal perturbations of OHC and SST are basin-scale anomalies (Figs. 3 and 4), the perturbations of MVT and MHT (e.g., with a 3-month delay) are coastally trapped anomalies extending along the eastern and western boundaries of the North Atlantic and positioned close to the latitudes where these two variables are measured in the model (i.e., 50° and 25°N; Figs. 5 and 6). To understand these differences we will now focus on MVT and OHC (since MHT and SST behave qualitatively similar to the former and the latter, respectively).

For MVT, the optimal perturbations combine temperature and salinity anomalies that constructively modify the density field (i.e., cold anomalies are accompanied by higher salinity). The induced density pattern is positive in the west of the basin and negative in the east, with virtually no signature in the interior (Fig. 5). The resulting density contrast across the basin induces an east–west baroclinic pressure difference that has to be balanced by a zonally averaged meridional geostrophic flow. Following Hirschi et al. (2003), $v \propto \partial_x P$, we have $\overline{v} \propto (P_{\mathrm{West}} - P_{\mathrm{st}})$, where v ($\overline{v}$) is the (zonally averaged) meridional velocity, P is pressure, x is the zonal direction, and P_{East} and P_{West} indicate pressure at the eastern and western boundaries of the basin, respectively. This flow alters MVT and MHT, which corresponds to the strengthening of the meridional overturning circulation. Since coastal ocean adjustment occurs significantly faster than the decadal time scale, this perturbation induces MVT and MHT changes almost instantaneously.

In contrast, the optimal perturbations of OHC combine temperature and salinity anomalies localized in the northwestern part of the North Atlantic basin adjacent to Canada, Greenland, and Iceland. These anomalies penetrate below the thermocline, reaching the maximum slightly below the thermocline (at ~1200 m) and persisting in the deep ocean (Fig. 3). These initial perturbations, when scaled to 1 mK, lead after 9.9 yr to an OHC anomaly of +12.6 mK. Stronger perturbations would lead to a proportionally stronger change in OHC.

The mechanism of the transient growth allowing such amplification of initial anomalies in the North Atlantic on decadal time scales has been previously identified by Sévellec and Fedorov (2015). They demonstrated that a positive surface density anomaly along the northwestern boundary of the North Atlantic, either a cooling or an increase of salinity or both, should lead to the strengthening of the AMOC after ~9 yr. They also showed that the density anomaly has to reach the deep ocean, penetrating below the thermocline, to be particularly efficient (Sévellec and Fedorov 2013b, 2015). The resulting strengthening of the AMOC is due to the efficient stimulation of large-scale baroclinic (thermal) Rossby waves, which induce an oscillation between MVT and OHC. This oscillation has a roughly 24-yr period and involves changes in MVT and OHC that are in quadrature (MVT > 0 → OHC > 0 → MVT < 0 → OHC < 0…; Sévellec and Fedorov 2013a).

Because of the different spatial scales of the optimal perturbations for OHC and MVT, the ocean response to these initial disturbances differs with time as well. Following (8), one can obtain a simple expression that describes the temporal evolution of any of the four variables after the initial disturbance is applied (at $t = 0$):

$$\langle \mathbf{F} \,|\, \mathbf{u}_\tau^{\mathrm{opt}}(t) \rangle = \langle \mathbf{F} | \mathbf{M}(t) | \mathbf{u}_\tau^{\mathrm{opt}}(0) \rangle . \qquad (10)$$

As expected, we find that each climate variable experiences the strongest increase when the system is perturbed by the LOPs computed for this particular variable (Fig. 7). However, MVT changes caused by its optimal perturbations are strongly damped just after

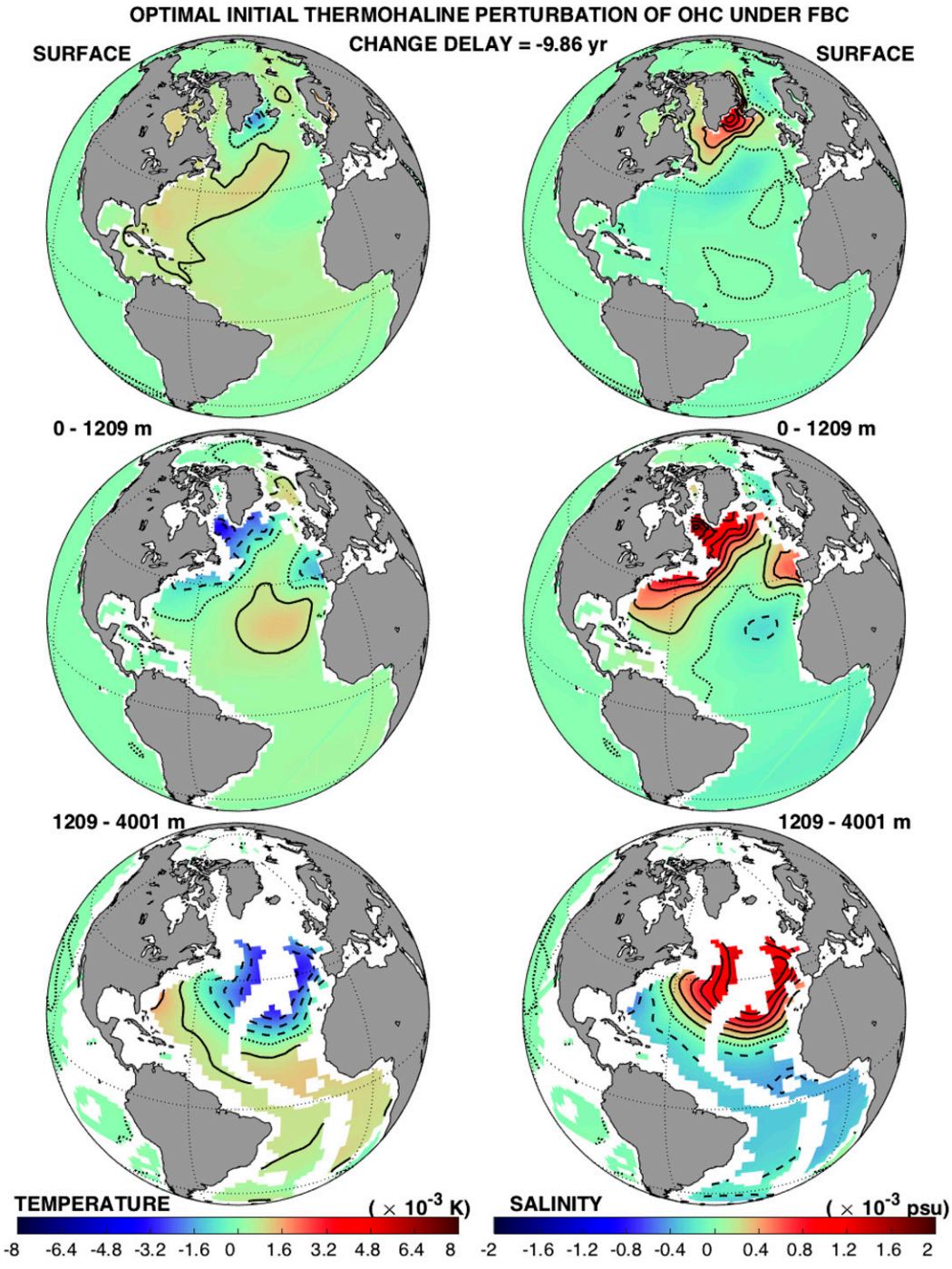

FIG. 3. The structure of the optimal initial thermohaline perturbation having the strongest impact on OHC after an optimal delay of 9.9 yr (i.e., the most efficient delay in Fig. 2d). This perturbation has an initial OHC anomaly on the order of −1 mK, but induces an anomaly of +15.6 mK after 9.9 yr. Note that temperature and salinity have a constructive (additive) effects on the initial density perturbation. The results are for the flux boundary conditions (FBC).

a few years, whereas OHC variations caused by its respective perturbations are only weakly damped (Figs. 7a,d). LOPs computed for one variable still perturb other variables. For example, the optimal perturbations of OHC lead to variations in MVT. These variations occur as a result of the excitation of the interdecadal oscillatory mode discussed in above (Sévellec and Fedorov 2013a). Because of their large spatial scales,

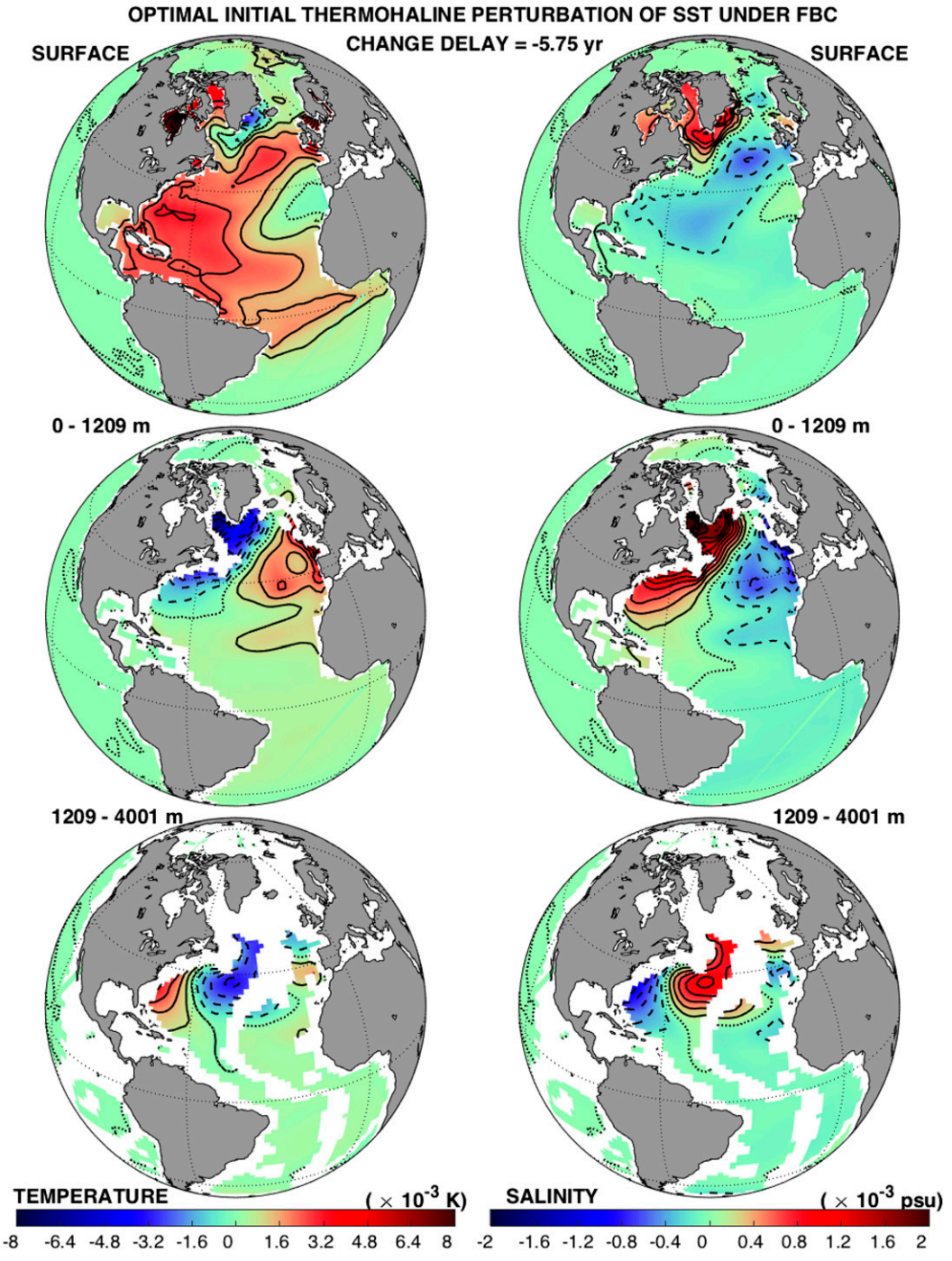

FIG. 4. As in Fig. 3, but for the optimal perturbation of spatially averaged SST and for an optimal delay of 5.8 yr (i.e., the most efficient delay in Fig. 2c). This perturbation has an initial anomaly in SST on the order of +1 mK, but induces an anomaly of +56 mK after 5.8 yr. The results are for the flux boundary conditions.

the optimal perturbations of OHC are more efficient for stimulating this mode.

The ocean response to the optimal perturbations of SST is generally similar to that of OHC, but the transient growth lasts a shorter time, and the oscillatory nature of the response is perhaps more noticeable (Fig. 7c). Like MVT, MHT shows a strongly damped response to its optimal perturbations (Fig. 7b), as the initial density anomalies have virtually no signature in the ocean interior that could support the signal on longer time scales.

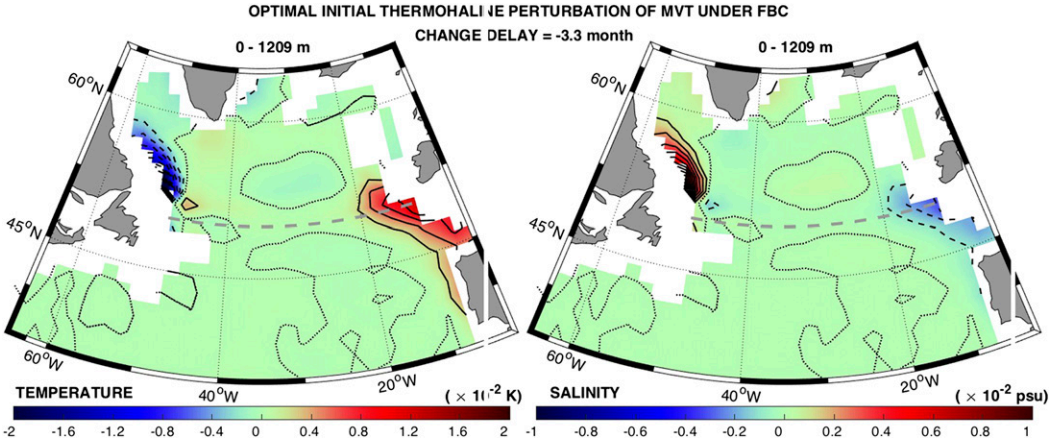

FIG. 5. The upper-ocean structure of the optimal thermohaline perturbation that has the largest impact on MVT after a delay of 3.3 months. Temperature and salinity are averaged between 0 and 1209 m. The light gray dashed line indicates the latitude at which MVT is estimated. Note the two coastally trapped waves located on the opposite sides of the basin; at time zero they will cross this latitude, leading to a large east–west density gradient and hence a net meridional geostrophic flow. The results are for the flux boundary conditions.

4. Idealized model

a. Idealized model formulation

So far we have demonstrated that MVT and OHC (or MHT and SST) exhibit dramatic differences in terms of sensitivity to the initial perturbations: meridional volume and heat transports are most sensitive to shorter time scales associated with smaller spatial-scale anomalies located near the basin western and eastern boundaries, whereas the two spatially averaged temperature variables are most sensitive to basin-scale anomalies which can induce transient growth up to a decade long. To further investigate the role of the horizontal length scale of the anomalies, specifically in controlling the time scale and maximum sensitivity for each of the four climatic variables, we use an idealized model of linear ocean dynamics formulated for the North Atlantic. The setting of the model (Fig. 8) is similar to that of Sévellec and Fedorov (2013a), Sévellec and Fedorov (2015), and Sévellec and Huck (2015), and the text below follows these studies with minor modifications.

The idealized model describes the linear dynamics of the ocean GCM with several approximations applied. For simplicity, we neglect the seasonal cycle and consider the system autonomous. Also, the large spatial scale of the problem allows us to reduce the momentum equations to geostrophic balance on a β plane (the planetary-geostrophic regime or the geostrophic regime of type 2; see Phillips 1963; Colin de Verdière 1988; Salmon 1998).

The model treats anomalies in temperature T' and salinity S' on two ocean levels, the top level (of depth h) and the deep level (of depth $\tilde{h}$). These anomalies are chosen to be functions of time t and the zonal coordinate x, and their evolution follows a set of advection–diffusion equations. To simplify the mathematical procedure of the analysis, meridional variations in T' and S' are neglected.

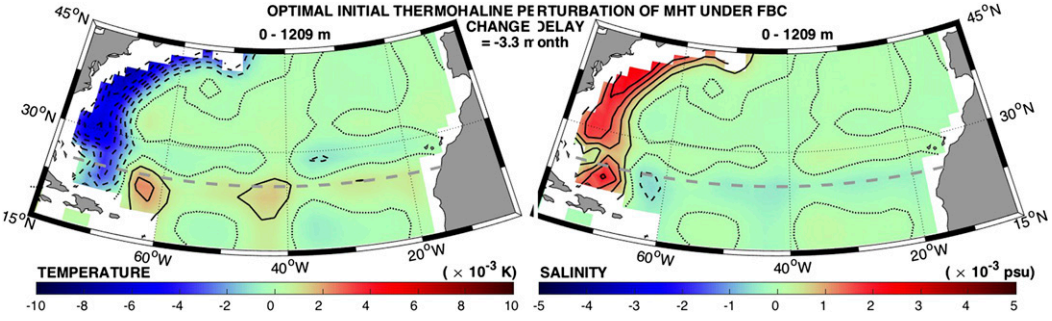

FIG. 6. As in Fig. 5, but for the optimal perturbation of MHT, also corresponding to a 3.3-month delay. The light gray dashed line indicates the latitude at which MHT is estimated. Note the coastally trapped wave on the western side of the basin that will cross this latitude at time zero. The results are for the flux boundary conditions.

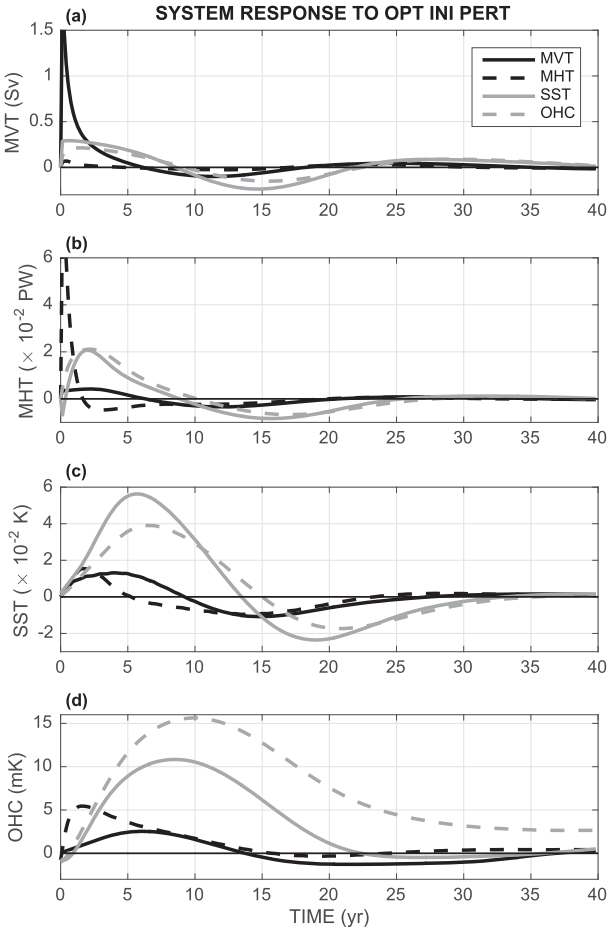

FIG. 7. The evolution of (a) MVT, (b) MHT, (c) SST, and (d) OHC in response to the optimal initial thermohaline perturbations specifically calculated for MVT (black solid line), MHT (black dashed line), SST (gray solid line), or OHC (gray dashed line). The spatial structure of the imposed initial temperature and salinity fields was shown in Figs. 5, 6, 4, and 3, respectively. Note the strongly damped oscillatory-like behavior with periodicity of about 24 years that occurs in many of these computations; it is related to the leading, interdecadal eigenmode of the system (Sévellec and Fedorov 2013a).

The zonal extent of the model basin is W; its full depth is H (numerical values of these and other parameters are given in Table 1).

The equations are linearized with respect to the mean state of the ocean. In particular, at the upper level we impose the mean zonal flow $\overline{u}$ and the mean temperature and salinity gradients. These gradients have meridional and vertical components: $\partial_y\{\overline{T}, \overline{S}\}$ and $\partial_z\{\overline{T}, \overline{S}\}$, where y and z are the meridional and vertical coordinates, and $\overline{T}$ and $\overline{S}$ are mean temperature and salinity, respectively. These gradients in the equations are approximated by simple constants obtained from the GCM output. In the deep ocean those constants are set to zero. Mean zonal gradients of temperature and salinity are neglected.

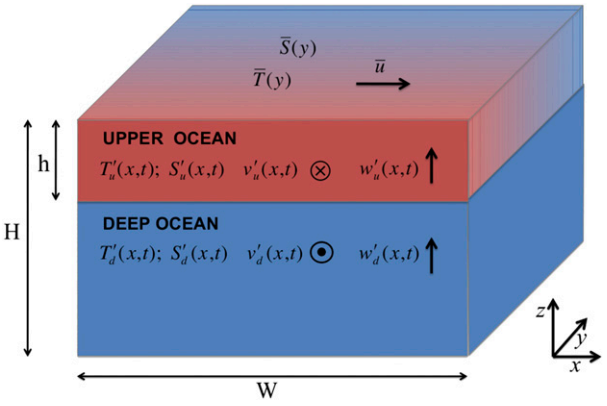

FIG. 8. A schematic of the idealized model. The two levels of the model represent the upper and deep ocean. The prognostic variables are temperature and salinity at each level (T'_u, S'_u, T'_d, and S'_d, respectively). The four diagnostic variables are meridional and vertical velocities, also at each level (v'_u, w'_u, v'_d, and w'_d). The model free parameters are the upper-ocean thickness h, the total ocean depth H, the zonal extent of the Atlantic basin W, the mean meridional flow $\overline{u}$, and the mean temperature and salinity fields ($\overline{T}$ and $\overline{S}$). For $\overline{T}$ and $\overline{S}$ we choose linear functions of y at the top level (both fields decreasing with latitude) and constants at the deeper level. Those constants are equal to the values of temperature and salinity in the upper ocean at the northern boundary of the basin. We also assume a nonzero vertical stratification in the upper layer that can support baroclinic Rossby waves due to the β effect. The dependence of the model variables on spatial coordinates (zonal—x, meridional—y, and vertical—z) and time t is shown in brackets. Color (blue to red) represents mean temperature variations (colder to warmer). A similar idealized model was used in Sévellec and Fedorov (2013a), Sévellec and Fedorov (2015), and Sévellec and Huck (2015).

For the prognostic variables of the model, we choose T'_u and S'_u, and T'_d and S'_d, which are temperature and salinity anomalies in the upper and deep oceans, respectively. These variables evolve according to the linearized advective–diffusion equations with horizontal diffusivity κ (see the appendix). The system is closed using thermal wind balance with a baroclinicity condition for the meridional velocity, a linear equation of state for seawater, a continuity equation, and the rigid-lid approximation.

The last step is to apply the Fourier transform along the zonal direction to T'_u, T'_d, S'_u, and S'_d, which yields, after some algebra, equations for the corresponding Fourier coefficients T'^u_{cn}, T'^u_{sn}, T'^d_{cn}, T'^d_{sn}, S'^u_{cn}, S'^u_{sn}, S'^d_{cn}, and S'^d_{sn}, where n indicates the wavenumber, u and d stand for the upper and deep model levels, and c and s for cosine and sine. These equations are summarized in the appendix and used in the analysis below. As shown by Sévellec and Fedorov (2013a) and Sévellec and Fedorov (2015), this idealized model is able to reproduce the dynamical behavior of the linear tangent and adjoint versions of the ocean GCM with the flux boundary

TABLE 1. Parameters of the idealized model.

h	1200 m	Model top level thickness
H	4500 m	Total ocean depth
W	60°	Basin zonal size
L	60°	Basin meridional size
κ	$2 \times 10^{3}\,\mathrm{m^2\,s^{-1}}$	Horizontal tracer diffusivity
g	$9.8\,\mathrm{m\,s^{-2}}$	Acceleration due to gravity
f	$10^{-4}\,\mathrm{s^{-1}}$	Coriolis parameter
β_f	$1.5 \times 10^{-11}\,\mathrm{m^{-1}\,s^{-1}}$	Latitudinal gradient of the Coriolis parameter (i.e., planetary vorticity gradient)
α	$2 \times 10^{-4}\,\mathrm{K^{-1}}$	Thermal expansion coefficient
β	$7 \times 10^{-4}\,\mathrm{psu^{-1}}$	Haline contraction coefficient
ΔT	−15 K	Mean meridional temperature contrast
ΔS	−1.5 psu	Mean meridional salinity contrast
$\bar{u}$	$2.5 \times 10^{-2}\,\mathrm{m\,s^{-1}}$	Mean zonal velocity in the upper ocean

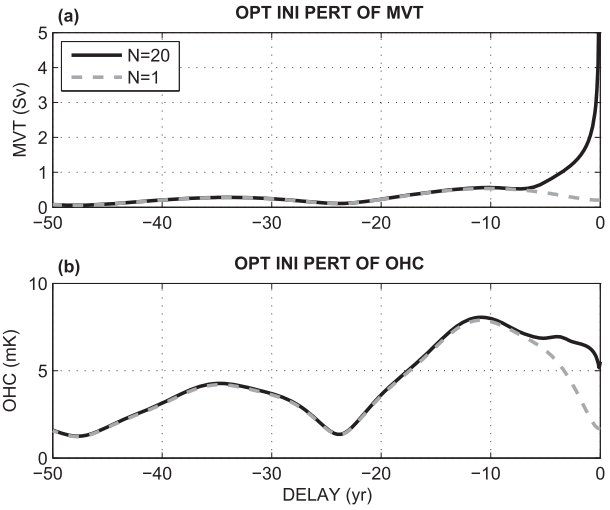

FIG. 9. The impact of the optimal initial perturbations of MVT and OHC on the respective variables as a function of the time delay τ, as obtained from the idealized model (cf. Fig. 2 for the ocean GCM). The impact is defined as the maximum magnitude that a particular variable would reach at the peak of the transient growth. Solid and dashed lines show results retaining 20 Fourier modes ($N = 20$; equivalent to a 3° zonal resolution) or just one ($N = 1$; the basin scale). Note that MVT is affected most efficiently by near-instantaneous perturbations ($\tau \simeq 0$); however, to capture this feature, one has to retain a sufficient number of Fourier modes. In contrast, OHC is most sensitive to past perturbations ($\tau \simeq -10$ yr), which remains true even if one severely truncates the Fourier expansion.

conditions. Those authors have also discussed the boundary conditions at the basin western and eastern boundaries required for such a model (restricting n to odd numbers).

Using this idealized spectral model we apply a similar optimization procedure as applied in section 3. For simplicity, here we will focus only on MVT and OHC, which show the highest sensitivity to small-scale instantaneous anomalies and basin-scale decadal anomalies, respectively.

b. Idealized model results

To investigate the role of the horizontal length scale of the optimal perturbations, especially their zonal scale, we have computed the LOPs of the idealized model for different values of N (from 1 to 20, where N is the number of the retained Fourier terms). Decreasing N is equivalent to applying a low-pass filter along the zonal direction, filtering smaller-scale anomalies. A Fourier series truncated at $N = 20$ would resolve roughly 3° of longitude (approaching the resolution of the ocean GCM).

First, let us consider the impacts of the optimal perturbations when we retain these first 20 Fourier terms in the expansion. In this case, the idealized model reproduces the delayed sensitivity of the full GCM very closely; OHC is most sensitive to initial perturbations after a roughly 10-yr delay, while MVT is sensitive to instantaneous perturbations (Fig. 9). Next, we compute LOPs but retain only the first Fourier term ($N = 1$, corresponding to the basin zonal length scale). Our computations reveal a striking difference: whereas the optimal perturbations of OHC are almost not affected by the filtering, the optimal perturbations of MVT show a much reduced sensitivity for instantaneous perturbations. In fact, the largest sensitivity is now for a 10-yr delay (Fig. 9, dashed line). This comparison of the filtered versus unfiltered computations confirms that OHC is primarily affected by large-scale anomalies whereas MVT is affected by all scales, including the smallest zonal scale in the model.

This particular behavior can be further analyzed by looking at the formulation of the cost function in the spectral model:

$$\mathrm{MVT} = \sum_{n=1}^{2N+1} \frac{gh\tilde{h}}{fH}\left[h\left(-\alpha T'^{u}_{\mathrm{cn}} + \beta S'^{u}_{\mathrm{cn}}\right) + \tilde{h}\left(-\alpha T'^{d}_{\mathrm{cn}} + \beta S'^{d}_{\mathrm{cn}}\right)\right],$$

$$\mathrm{OHC} = \sum_{n=1}^{2N+1} \frac{2}{n\pi H}\left(hT'^{u}_{\mathrm{sn}} + \tilde{h}T'^{d}_{\mathrm{sn}}\right).$$

Whereas MVT is independent of the wavenumber n, OHC is inversely proportional to it. This means that potentially each Fourier mode has similar impacts on MVT, increasing its overall sensitivity to perturbations. At short times, when smaller-scale anomalies are not yet damped by horizontal diffusion, it is the cumulative effect of all spatial scales that controls MVT anomalies, which makes instantaneous values of MVT virtually unpredictable. On the other hand, OHC is inversely proportional to the wavenumber, with smaller sensitivity to high wavenumbers (i.e., small-scale anomalies). This

TABLE 2. Characteristics of the most efficient transient change for optimal initial perturbations corresponding to different measures and scaled to the order of 1 mK (i.e., $\alpha^{-1}\sqrt{\langle \mathbf{u}(0)|\mathbf{S}|\mathbf{u}(0)\rangle} = 10^{-3}$ K). Values in bold indicate experiments with the strongest impact. Climatic error bounds are defined after applying a 30-yr averaging to the relevant variables.

Optimization measure	Boundary conditions	Most efficient time delay	Absolute error bound	Normalized error bound	Absolute climatic error bound	Normalized climatic error bound
MVT	FBC	≥ -0.1 yr	± 2.2 Sv	**128%**	± 0.36 Sv	**61%**
	MBC	≥ -0.1 yr	± 2.2 Sv	128%	± 0.30 Sv	51%
MHT	FBC	≥ -0.1 yr	$\pm 9.8 \times 10^{-2}$ PW	**144%**	$\pm 1.5 \times 10^{-2}$ PW	**71%**
	MBC	≥ -0.1 yr	$\pm 9.8 \times 10^{-2}$ PW	144%	$\pm 1.4 \times 10^{-2}$ PW	64%
SST	FBC	-5.8 yr	$\pm 5.6 \times 10^{-2}$ K	**24%**	$\pm 4.4 \times 10^{-2}$ K	**45%**
	MBC	≥ -0.1 yr	$\pm 1.5 \times 10^{-2}$ K	6.4%	$\pm 1.0 \times 10^{-2}$ K	9%
OHC	FBC	-9.9 yr	± 15.6 mK	**34%**	± 12.6 mK	**42%**
	MBC	-9.4 yr	± 12.2 mK	26%	± 10.4 mK	35%

fundamental difference between MVT and OHC comes from the fact that the former depends of the east–west temperature difference (assuming geostrophic balance, MVT $\propto \int_{\text{East}}^{\text{West}} v'\,dx \propto \rho_{\text{West}} - \rho_{\text{East}}$, where v' is the anomalous meridional flow, x is the zonal coordinate, and ρ_{East} and ρ_{West} are density anomalies at the eastern and western boundaries, respectively). In contrast, the latter is an integral of temperature (OHC $\propto \int_{\text{East}}^{\text{West}} T'\,dx$), which filters out small-scale sensitivity. Thus, MVT is more sensitive to smaller scales than OHC.

Thus, only if one restricts consideration to basin-scale anomalies, MVT and OHC behave similarly (dashed gray lines in Fig. 9). In that case, LOPs of both variables induce optimal transient change on a decadal time scale, following the mechanism discussed in Sévellec and Fedorov (2013b) and Sévellec and Fedorov (2015). This transient change corresponds to the nonnormal stimulation of a 24-yr oscillatory eigenmode (Sévellec and Fedorov 2013a), whose signature is evident for example in the oscillatory-like variations in sensitivity in Fig. 9.

5. Implications for predictability of the ocean state

We now return to the results of the ocean GCM and examine their implications for the predictability of the ocean state in the North Atlantic described in terms of the four climate variables under consideration. In fact, whether an optimal delay exists or not has direct consequences for the predictability of the system. Since optimal initial anomalies with an average magnitude of just a few mK (in the norm sense) are able to significantly modify the chosen ocean state metrics, the optimal time delays for each particular metric sets a potential time limit on its predictability. Note that the maximum values of these initial anomalies remain below 10^{-2} K, far below the accuracy of ocean measurements. In this sense, SST and OHC are predictable up to 6 and 10 yr, respectively, but instantaneous values of MVT and MHT are unpredictable (as errors projecting on the optimal perturbations can impact the latter variables almost immediately).

To further quantify the system predictability, we compare the maximum impact of the initial perturbations (scaled to 1 mK) to the typical magnitude of variability of each metric in a full climate GCM. Accordingly, we define the normalized error bound as the ratio between the former and the latter. The coupled model we use is IPSL-CM5, which employs the same ocean model with the same configuration (Marti et al. 2010) as the present study.

Following (9), the error bound (i.e., the maximum impact of an optimal perturbation on a particular measure) can be computed as $\max_\tau\left[\epsilon\sqrt{\langle \mathbf{F}|\mathbf{M}(-\tau)\mathbf{P}\mathbf{N}^{-1}\mathbf{P}^\dagger\mathbf{M}^\dagger(\tau)|\mathbf{F}\rangle}\right]$, with $\varepsilon/\alpha = 10^{-3}$ K (Table 2). The magnitude of variability of each measure can be estimated as the standard deviation of its annual-mean value from a 1000-yr-long preindustrial simulation of the IPSL model (Dufresne et al. 2013; Mignot and Bony 2013). The ratio of the error bound to the standard deviation yields the normalized error bound.

We obtain that the normalized error bound exceeds 100% for MVT and MHT but stays below 40% for SST and OHC. Such strong relative impacts of small disturbances (1 mK) compared to the overall variability confirm lower predictability of MVT and MHT. For OHC the normalized error bound reaches only 34%, suggesting higher predictability. The effect on these results of changing the type of surface boundary conditions is small (Table 2). However, one should keep in mind that these numbers are important only in a relative sense, since the initial disturbances could be scaled by an arbitrary factor. Another critical factor relevant to these results is the extent to which the spatial structure of the noise actually present in the ocean model or in nature would project onto the optimal perturbations.

For SST, variability in the climate model is strongly affected by atmospheric processes, absent in the forced context, which could artificially reduce the normalized

error bound. Keeping in mind this limitation, our result suggest that small disturbances in the ocean model can lead to an SST change comparable to the overall SST variability in the climate model (i.e., a 4-mK anomaly leading to a normalized error bound of nearly 100% for the flux boundary conditions).

Thus far, the cost function has been defined using instantaneous measurements. However, for climatic purposes one would like to predict a time average of each metric rather than its instantaneous value. To test how time averaging would modify the system sensitivity to small disturbances and hence its predictability, we now compute the error bound for a time-averaged cost function:

$$\langle \mathbf{F}|\mathbf{u}\rangle = \begin{cases} \langle \mathrm{MVT}\rangle_{\Pi} = \displaystyle\int_{t_m-\Pi}^{t_m}\int_{z_{\max(\overline{\mathrm{MVT}})}}^{0}\int_{x_W}^{x_E} v|_{y_{\max(\overline{\mathrm{MVT}})}}\, dx\, dz\, dt, \\ \langle \mathrm{MHT}\rangle_{\Pi} = \displaystyle\int_{t_m-\Pi}^{t_m}\iint_{\Sigma} vT|_{y_{\max(\overline{\mathrm{MHT}})}}\, d\sigma\, dt, \\ \langle \mathrm{SST}\rangle_{\Pi} = \displaystyle\int_{t_m-\Pi}^{t_m}\frac{1}{S_{\mathrm{NA}}}\iint_{\mathrm{NA}} T|_{z=0}\, ds\, dt, \\ \langle \mathrm{OHC}\rangle_{\Pi} = \displaystyle\int_{t_m-\Pi}^{t_m}\frac{1}{V_{\mathrm{NA}}}\iiint_{\mathrm{NA}} T\, dv\, dt, \end{cases} \tag{11}$$

where Π is the length of the time averaging interval (we use Π in the range 1 to 40 yr). As in the previous analysis, the effect of averaging strongly differs for MVT and MHT versus SST and OHC (Fig. 10). For the former metrics, as the length of the time averaging increases the influence of LOPs decreases, suggesting a better predictability. However, for the latter metrics, the time averaging does not affect the impacts of LOPs much, so that their predictability does not change.

We now define the climatic error bound as the maximum impact of a LOP on a 30-yr average of a particular metric. The choice of $\Pi = 30$ yr is somewhat arbitrary, corresponding to a traditional definition of "climate." Going from the error bound to the climatic error bound shows a dramatic decrease in the impact of LOPs by a factor of 5 for MVT and MHT, but no significant change for SST and OHC (Table 2).

To further assess the relative impact of small disturbances, for each metric we compare the error bound computed for different time averages with their standard deviation in the IPSL model also computed using different durations of the running average. As previously, we estimate the ratio of the two and define the normalized climatic error bound (Fig. 11). For MVT and MHT, the normalized error bound shows an overall

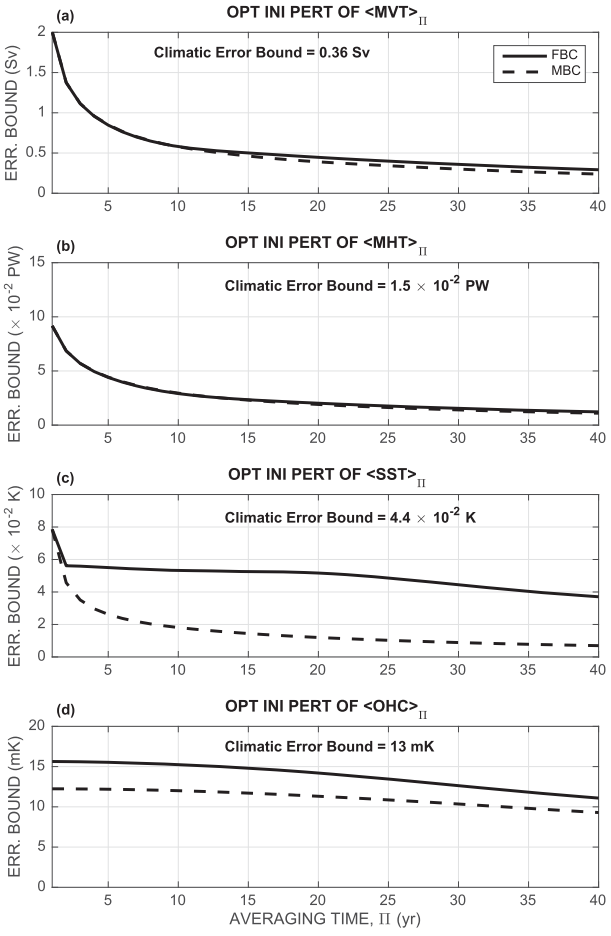

FIG. 10. (a)–(d) Error bound (i.e., the maximum impact of the respective optimal initial perturbation) as a function of the averaging time Π applied to MVT, MHT, SST, and OHC. These averaged variables are denoted as $\langle \mathrm{MVT}\rangle_{\Pi}$, for example. Solid and dashed lines represent different boundary conditions (FBC and MBC, respectively). For $\Pi = 0$ the values of the error bound would be the same as the maximum values in Fig. 2. The climatic error bound is defined as the error bound for time averages with $\Pi = 30$ yr.

decrease for longer averaging intervals, leading to the values of the normalized climatic error bound (defined for $\Pi = 30$ yr) at 60% and 70%, respectively. For MVT there exists a best averaging interval of about 10 yr with a normalized climatic error bound of 50%, suggesting a "sweet spot" for MVT predictability. For MHT, the longer the averaging interval is, the better.

For OHC, the results are only weakly dependent on the duration of the averaging, except for a weak local maximum (i.e., a worst case in terms of prediction) around 20 yr. The normalized climatic error bound is about 40%. Overall, both MVT and MHT seem to become more predictable when a long time average is used, whereas OHC predictability changes very little (Fig. 11d). For SST, different types of surface boundary

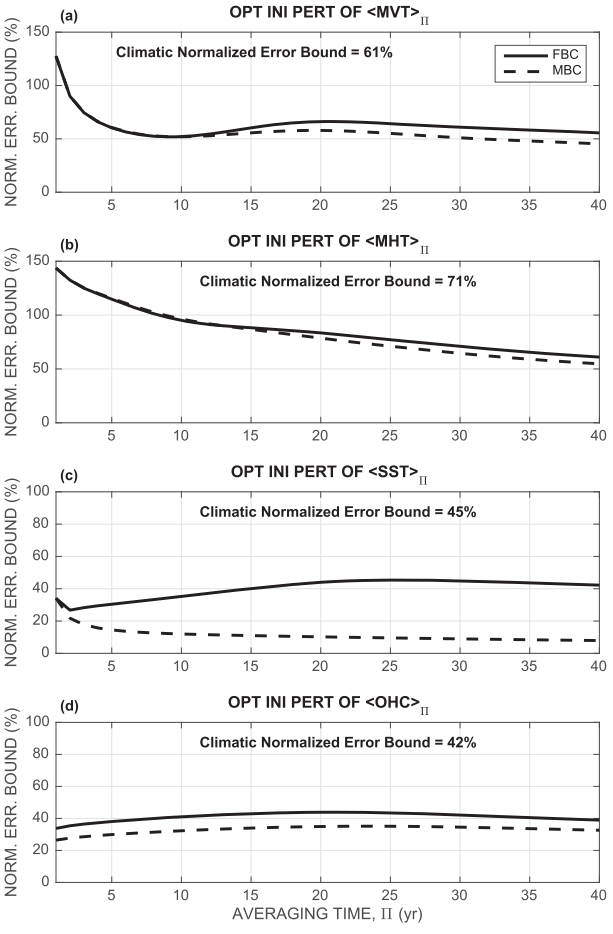

FIG. 11. As in Fig. 10, but normalized with the standard deviation of time averages of each variable in a fully coupled model (IPSL-CM5). The climatic normalized error bound is defined as the normalized error bound for time averages with $\Pi = 30$ yr.

conditions produce rather different results (Fig. 11c), suggesting that this issue should be considered in a fully coupled model.

6. Discussion and conclusions

The climate system exhibits variability on time scales ranging from synoptic to interannual and decadal to centennial and much longer (Ghil 2002). These different time scales modulate one another; for example, the activity of tropical cyclones is modulated on decadal time scales by the Atlantic multidecadal variability (Goldenberg et al. 2001; Delworth and Mann 2000). Thus, to predict changes in weather pattern or the occurrence of extreme events, we need to improve our ability to predict decadal climate variations.

On such decadal time scales, model initial conditions are critical for prediction (as opposed to a particular CO_2 emission scenario more relevant on centennial time scale; Hawkins and Sutton 2009b). However, since the climate system is chaotic, any errors in the estimate of these initial can lead in time to significant errors in both the phase and amplitude of the signal, following the same principle as the well-known "butterfly effect" for the atmosphere (Lorenz 1963).

To that end, here we have determined the time scale and intensity of the transient growth of initial disturbances of the North Atlantic Ocean state within a forced ocean model framework. The next question is how fast and how strongly these initial errors can modify the ocean state, thus setting a limit on ocean predictability. Answering this question, we have assessed the sensitivity to initial conditions of four metrics of the North Atlantic Ocean state: meridional volume transport (MVT at 50°N and 1500-m depth), meridional heat transport (MHT at 25°N), sea surface temperature (SST averaged between 30° and 70°N), and ocean heat content (OHC averaged between 30° and 70°N and with depths). We have followed the generalized stability analysis (Farrell and Ioannou 1996a,b) but have reshaped it for the purpose of looking at linear measures of the ocean state, as suggested by Sévellec et al. (2007). This method involves the computation of LOPs (linear optimal perturbations) obtained by maximizing a Lagrangian function, which requires the use of an adjoint to the ocean GCM (Sévellec and Fedorov 2015).

We have demonstrated that ocean predictability strongly depends on the metrics chosen to evaluate the ocean state. For instance, metrics corresponding to large spatial scales, such as the spatially averaged ocean heat content and SST, have predictability of 10 and 6 yr, respectively. On the other hand, instantaneous values of meridional volume and heat transports, which can be strongly influenced by processes at the boundaries of the basin, do not show any predictability. We have rationalized this result using an idealized ocean model.

These findings are generally consistent with the 7.5-yr optimal transient growth for the AMOC intensity obtained by Zanna et al. (2011) in an ocean model using an idealized configuration (a rectangular basin with flat bottom). However, those authors applied a different metric for the AMOC volume transport by averaging the streamfunction meridionally and vertically. Such spatial averaging filters out the effect of small-scale disturbances. Hence, their metric becomes more comparable to our SST and OHC metrics (also based on spatial averages). As discussed in our study, the averaging leads to a higher sensitivity to past disturbances than to instantaneous disturbances.

In our study, we have shown that the ocean predictability is indeed controlled by the transient growth of small perturbations. These perturbations can grow

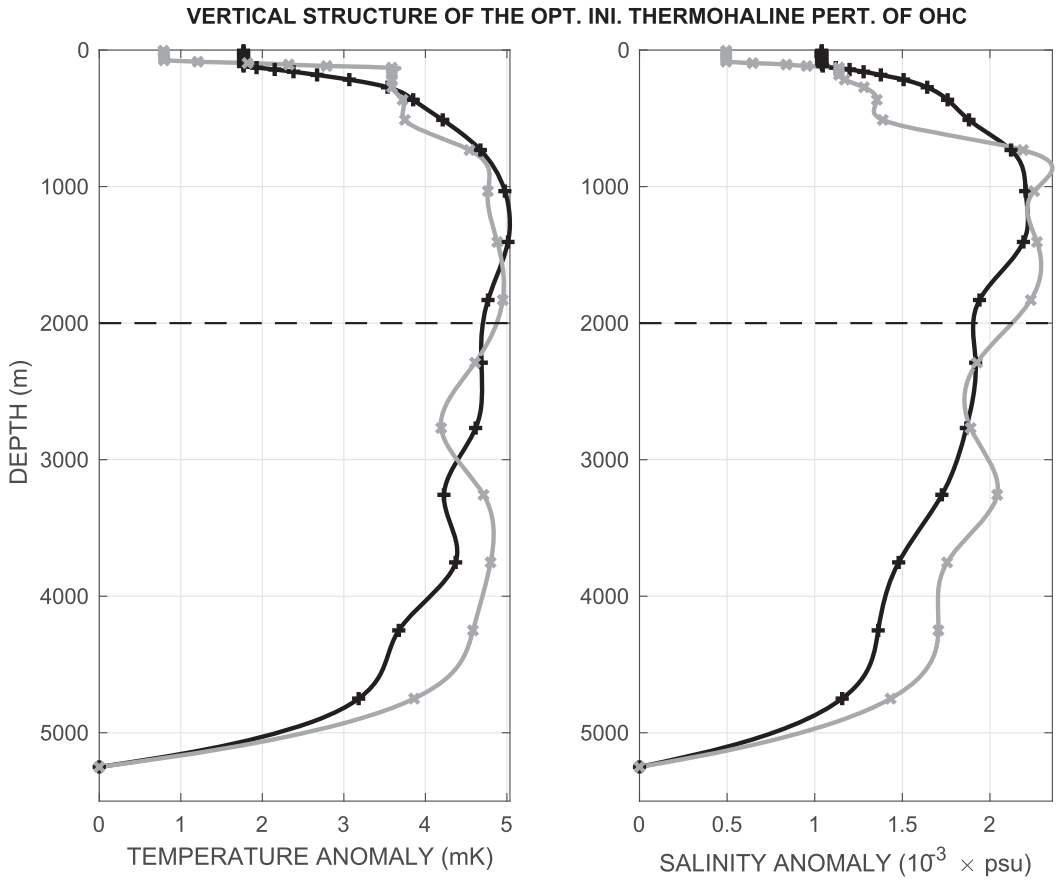

FIG. 12. The vertical structure and magnitude of the optimal initial perturbations for OHC under FBC (thick black lines; full structure shown in Fig. 3) and MBC (thick gray lines) as a function of depth. Crosses indicate the maximum values of (left) temperature and (right) salinity anomalies at each level of the ocean GCM and are connected by a cubic spline interpolation. The horizontal dashed line indicates the typical depth limit of Argo floats (2000 m). In effect, this plot shows the sensitivity of North Atlantic Ocean heat content to past disturbances at different depths. The strongest sensitivity develops for disturbances located at a depth between 1000 and 2000 m. The net system sensitivity associated with the deep ocean (below 2000 m) is comparable to if not greater than that associated with the upper ocean (above 2000 m). Note that the relative differences in sensitivity for different surface boundary conditions (FBC and MBC) become small below several hundred meters.

significantly, so that the characteristic time scale of the transient growth sets the limit of predictability of the system. A complementary analysis (Sévellec and Fedorov 2013b) demonstrated that the transient growth time scale is given by the damping time scale due to horizontal diffusion limiting the residence time scale of deep ocean perturbations. This damping affects differently perturbations having small and large spatial scales, as expected from the Laplace operator of diffusion ($\tau \propto \lambda^2$, where τ is the diffusive time scale and λ is the spatial scale of the perturbation). Thus, the metrics influenced by perturbations with smaller spatial scales (e.g., MVT and MHT) have a shorter predictability, whereas metrics predominantly influenced by large-scale anomalies (e.g., SST and OHC) can have longer predictability. Since small spatial scales in the ocean are given by the internal Rossby radius of deformation, in principle this makes instantaneous values of MVT and MHT unpredictable. In contrast, the largest spatial scale being the basin size implies longer predictability for SST and OHC limited by a potential predictability barrier at roughly 6 and 10 yr, respectively. For SST, however, this result might change in a coupled ocean–atmosphere context due to the competing effects of active ocean–atmosphere coupling, if any is present, and atmospheric stochastic noise.

In general, applying time averaging to the metrics enhances their predictability in comparison to their instantaneous values. It is especially true for MVT and MHT, for which time averaging filters out dependency on small-scale perturbations and increases predictability by more than a factor of 4 (in terms of error growth) when these two metrics are averaged over 30 yr.

Nevertheless, when compared to variability in a climate model (i.e., IPSL-CM5; Dufresne et al. 2013; Mignot and Bony 2013), all 30-yr averaged metrics show a relatively weak predictability (despite a local optimal for MVT for the averaging interval of 10 years). Indeed, initial perturbations of only 1 mK can lead on decadal time scale to anomalies reaching roughly 60% and 40% of the MVT and OHC standard deviation, respectively. Whether this result makes these variables unpredictable in practice, in view of the typical uncertainty of temperature measurements, depends on the extent to which errors in the initial conditions would project onto the optimal perturbations.

In addition, we find that, regardless of the surface boundary conditions used, the four climate metrics under consideration have sensitivity to initial perturbations in the deep ocean (below 2000 m) as large as that to initial perturbations in the upper ocean (in the top 2000 m) (see Fig. 12). This finding, consistent with the previous results of Sévellec and Fedorov (2013b), stresses the need for accurate measurements in the deep ocean below the normal depth limit of ARGO floats.

To test the robustness of our results we have compared the impacts of two different types of surface boundary conditions for the ocean model: the mixed and flux boundary conditions (the former use a restoring term for temperature). We find that, except for the SST metric, the results are only weakly modified by the choice of the boundary conditions. This gives us more confidence in our results for the MVT, MHT, and OHC metrics. However, the results for SST do depend on the boundary conditions, which implies that ocean–atmosphere coupling can become a defining factor for this metric. The SST metric is arguably the most important for climate prediction, since it directly influences surface air temperature.

By construction, our forced ocean framework disregards potential effects of large-scale active ocean–atmosphere coupling (passive coupling is included in the mixed boundary conditions) and stochastic noise linked to atmospheric synoptic variability. Whereas the former can be a source of predictability, the latter contributes to error growth. Thus, in the future we intend to extend our analysis to a fully coupled ocean–atmosphere context. Note, however, that the results of our ongoing work on testing the LOPs of North Atlantic Ocean heat content in a coupled GCM do suggest that the general development in the first two decades still follows closely the predictions of the linear, ocean-only computations with a modified surface temperature damping coefficient as long as the imposed initial perturbations are relatively small (e.g., comparable to the coupled model internal variability; A. Germe et al. 2016, unpublished manuscript).

Finally, while the results of this study have been obtained by linearizing the primitive equations of motion around the model climatological basic state, it could be useful to test their robustness using a more variable model background state. This can be done by computing the model trajectory using surface boundary conditions based on historical observations (as opposed to the climatological forcing in the present study). Also, the results of this study could be extended to a fully nonlinear framework. Specifically, conditional nonlinear optimal perturbations (Mu and Zhang 2006; Zu et al. 2013; Li et al. 2014) provide a natural extension of the LOPs. Together with considering the effects of ocean–atmosphere coupling, these ideas will offer directions for future work.

Acknowledgments. This research was supported by grants from the DOE Office of Science (DE-SC0016538), the National Science Foundation (AGS-1405272), the National Oceanic and Atmospheric Administration (NA14OAR4310277), and the Natural and Environmental Research Council UK (MESO-CLIP, NE/K005928/1 and SMURPHS, NE/N005767/1). Support from the Yale University High Performance Computing facilities is also acknowledged. We thank Brian Dobbins for his help with setting up numerical experiments.

APPENDIX

Details of the Idealized Model

a. Equations

We describe here the idealized model used in section 4 in more detail. The setting of the model follows that of Sévellec and Fedorov (2013a), Sévellec and Fedorov (2015), and Sévellec and Huck (2015) and is provided here for completeness. However, whereas Sévellec and Fedorov (2013a) investigated the existence and properties of the least-damped, interdecadal AMOC eigenmode and how this mode can be excited most efficiently, here we focus on how initial disturbances can affect different measures of the North Atlantic Ocean state, following more closely Sévellec and Fedorov (2015). This problem deals with transient behavior of the system and requires a specific approach in view of the system nonnormality.

As discussed in section 4, for the prognostic variables of the two-layer model, we choose T'_u and S'_u, and T'_d and S'_d, which are temperature and salinity anomalies in the upper and deep oceans, respectively. These variables evolve according to linearized advective–diffusion equations with horizontal diffusivity κ:

$$\partial_t T'_u = -\overline{u}\partial_x T'_u - v'_u \partial_y \overline{T} - w'_u \partial_z \overline{T} + \partial_x(\kappa \partial_x T'_u), \quad \text{(A1a)}$$

$$\partial_t S'_u = -\overline{u}\partial_x S'_u - v'_u \partial_y \overline{S} - w'_u \partial_z \overline{S} + \partial_x(\kappa \partial_x S'_u), \quad \text{(A1b)}$$

$$\partial_t T'_d = \partial_x(\kappa \partial_x T'_d), \quad \text{(A1c)}$$

$$\partial_t S'_d = \partial_x(\kappa \partial_x S'_d), \quad \text{(A1d)}$$

where v'_u and w'_u are the meridional and vertical velocities in the upper ocean.

The system is closed using thermal wind balance with a baroclinicity condition for the meridional velocity, a linear equation of state for seawater, a continuity equation, and the rigid-lid approximation:

$$\partial_z v' = \frac{g}{f}(\alpha \partial_x T' - \beta \partial_x S'), \quad \text{(A2a)}$$

$$\int_{-H}^{0} v' \, dz = 0, \quad \text{(A2b)}$$

$$\partial_y v' + \partial_z w' = 0, \quad \text{with} \quad w'|_{z=0} = 0, \quad \text{(A2c)}$$

where v' and w' are the meridional and vertical velocities; both are functions of x, y and z. Also, f is the Coriolis parameter, g is the acceleration of gravity, α is the thermal expansion coefficient, and β is the haline contraction coefficient (the numerical values of these parameters are given in Table 1). To obtain the meridional and vertical velocity at the upper level, we vertically discretize the latter set of equations on the upper and deep levels using the Arakawa C grid (together with simple linear interpolations between the missing values, if needed).

Using the Fourier coefficients with respect to x, we express temperature and salinity anomalies as

$$T'_{\{u,d\}} = \sum_n T'^{\{u,d\}}_{cn} \cos\left(\frac{n\pi}{W}x\right) + T'^{\{u,d\}}_{sn} \sin\left(\frac{n\pi}{W}x\right),$$

$$S'_{\{u,d\}} = \sum_n S'^{\{u,d\}}_{cn} \cos\left(\frac{n\pi}{W}x\right) + S'^{\{u,d\}}_{sn} \sin\left(\frac{n\pi}{W}x\right).$$

We apply this Fourier transform with respect to x to the set of (A1a)–(A1d); using (A2) reduces the idealized model to

$$d_t|\mathbf{u}_{\text{id}}\rangle = \mathbf{A}_{\text{id}}|\mathbf{u}_{\text{id}}\rangle, \quad \text{(A3)}$$

with

$$\langle \boldsymbol{u}_{\text{id}}| = (T'^{u}_{\text{cn}}, T'^{u}_{\text{sn}}, T'^{d}_{\text{cn}}, T'^{d}_{\text{sn}}, S'^{u}_{\text{cn}}, S'^{u}_{\text{sn}}, S'^{d}_{\text{cn}}, S'^{d}_{\text{sn}}),$$

and

$$\mathbf{A}_{\text{id}} = \begin{pmatrix}
-\kappa\left(\frac{n\pi}{W}\right)^2 & A_{1,2} - \frac{n\pi}{W}\overline{u} & 0 & A_{1,4} & 0 & A_{1,6} & 0 & A_{1,8} \\
A_{2,1} + \frac{n\pi}{W}\overline{u} & -\kappa\left(\frac{n\pi}{W}\right)^2 & A_{2,3} & 0 & A_{2,5} & 0 & A_{2,7} & 0 \\
0 & 0 & -\kappa\left(\frac{n\pi}{W}\right)^2 & 0 & 0 & 0 & 0 & 0 \\
0 & 0 & 0 & -\kappa\left(\frac{n\pi}{W}\right)^2 & 0 & 0 & 0 & 0 \\
0 & A_{5,2} & 0 & A_{5,4} & -\kappa\left(\frac{n\pi}{W}\right)^2 & A_{5,6} + \frac{n\pi}{W}\overline{u} & 0 & A_{5,8} \\
A_{6,1} & 0 & A_{6,3} & 0 & A_{6,5} - \frac{n\pi}{W}\overline{u} & -\kappa\left(\frac{n\pi}{W}\right)^2 & A_{6,7} & 0 \\
0 & 0 & 0 & 0 & 0 & 0 & -\kappa\left(\frac{n\pi}{W}\right)^2 & 0 \\
0 & 0 & 0 & 0 & 0 & 0 & 0 & -\kappa\left(\frac{n\pi}{W}\right)^2
\end{pmatrix},$$

where T'^{u}_{cn}, T'^{u}_{sn}, T'^{d}_{cn}, T'^{d}_{sn}, S'^{u}_{cn}, S'^{u}_{sn}, S'^{d}_{cn}, and S'^{d}_{sn} are the Fourier coefficients, $|\mathbf{u}_{\text{id}}\rangle$ is the state vector, and $\mathbf{A}_{\text{id}}$ is the Jacobian matrix of the idealized model. Here, n (=1, 3, 5...) indicates the wavenumber, u and d stand for the upper and deep levels, and c and s for cosine and sine. The nonzero terms in this matrix correspond to diffusion, advection by the mean flow, geostrophic self-advection, and the baroclinic Rossby wave propagation. The terms describing the two latter effects are calculated as

$$A_{1,2} = -A_{2,1} = \frac{h}{\tilde{h}}A_{1,4} = -\frac{h}{\tilde{h}}A_{2,3} = -\frac{n\pi}{W}\left(\frac{\alpha g \tilde{h} h}{2Hf}\partial_y \overline{T} - \frac{\alpha g \tilde{h} h^2 \beta_f}{4Hf^2}\partial_z \overline{T}\right),$$

$$
\begin{aligned}
A_{1,6} &= -A_{2,5} = \frac{h}{\tilde{h}} A_{1,8} = -\frac{h}{\tilde{h}} A_{2,7} \\
&= +\frac{n\pi}{W}\left(\frac{\beta g\tilde{h}h}{2Hf}\partial_y \overline{T} - \frac{\beta g\tilde{h}h^2\beta_f}{4Hf^2}\partial_z \overline{T}\right), \\
A_{5,6} &= -A_{6,5} = \frac{h}{\tilde{h}} A_{5,8} = -\frac{h}{\tilde{h}} A_{6,7} \\
&= +\frac{n\pi}{W}\left(\frac{\beta g\tilde{h}h}{2Hf}\partial_y \overline{S} - \frac{\beta g\tilde{h}h^2\beta_f}{4Hf^2}\partial_z \overline{S}\right), \\
A_{5,2} &= -A_{6,1} = \frac{h}{\tilde{h}} A_{5,4} = -\frac{h}{\tilde{h}} A_{6,3} \\
&= -\frac{n\pi}{W}\left(\frac{\alpha g\tilde{h}h}{2Hf}\partial_y \overline{S} - \frac{\alpha g\tilde{h}h^2\beta_f}{4Hf^2}\partial_z \overline{S}\right),
\end{aligned}
$$

where $\tilde{h} = H - h$ is the thickness of the deep level, and $\beta_f = d_y f$ is the meridional gradient of the Coriolis parameter estimated for the northern Atlantic (between 30° and 60°N).

b. Optimization

To understand the transient behavior of the idealized model, we now perform a generalized stability analysis following the procedure outlined in section 3a. To that end, we need to define (i) the measure of the optimization problem or the cost function and (ii) an appropriate norm for the initial anomalies, both in the context of the idealized model.

Accordingly, we define the operator $\langle \mathbf{F}_{\mathrm{id}}|$ for MVT and OHC as

$$
\langle \mathbf{F}_{\mathrm{id}}| = \begin{cases} \displaystyle\sum_{n=1}^{2N+1} \frac{gh\tilde{h}}{fH}(-\alpha h, 0, -\alpha\tilde{h}, 0, \beta h, 0, \beta\tilde{h}, 0) \text{ for MVT, and} \\ \displaystyle\sum_{n=1}^{2N+1} \frac{2}{n\pi H}(0, h, 0, \tilde{h}, 0, 0, 0, 0) \text{ for OHC.} \end{cases}
$$

The norm, $\mathbf{S}_{\mathrm{id}}$, is chosen as

$$
\begin{aligned}
\langle \mathbf{u}_{\mathrm{id}}|\mathbf{S}_{\mathrm{id}}|\mathbf{u}_{\mathrm{id}}\rangle &= \frac{h}{H}(\alpha^2 T_{\mathrm{cn}}^{u2} + \alpha^2 T_{\mathrm{sn}}^{u2} + \beta^2 S_{\mathrm{cn}}^{u2} + \beta^2 S_{\mathrm{sn}}^{u2}) \\
&\quad + \frac{\tilde{h}}{H}(\alpha^2 T_{\mathrm{cn}}^{d2} + \alpha^2 T_{\mathrm{sn}}^{d2} + \beta^2 S_{\mathrm{sn}}^{d2} + \beta^2 S_{\mathrm{sn}}^{d2}).
\end{aligned} \tag{A4}
$$

To test the role of the horizontal scales for the solution, we solve the optimization problem truncating the Fourier expansion using different total number of waves ($N = 1$, and $N = 20$). Note that $N = 20$ corresponds to a 3° resolution, close to the GCM resolution used in this study; $N = 1$ can describe only the basin scale. The results of the optimization analysis are discussed in section 4.

REFERENCES

Arzel, O., T. Huck, and A. Colin de Verdière, 2006: The different nature of the interdecadal variability of the thermohaline circulation under mixed and flux boundary conditions. *J. Phys. Oceanogr.*, **36**, 1703–1718, doi:10.1175/JPO2938.1.

Baehr, J., and R. Piontek, 2014: Ensemble initialization of the oceanic component of a coupled model through bred vectors at seasonal-to-interannual timescales. *Geosci. Model Dev.*, **7**, 453–461, doi:10.5194/gmd-7-453-2014.

Blanke, B., and P. Delecluse, 1993: Variability of the tropical Atlantic Ocean simulated by a general circulation model with two different mixed-layer physics. *J. Phys. Oceanogr.*, **23**, 1363–1388, doi:10.1175/1520-0485(1993)023<1363:VOTTAO>2.0.CO;2.

Branstator, G., and H. Teng, 2014: Is AMOC more predictable than North Atlantic heat content? *J. Climate*, **27**, 3537–3550, doi:10.1175/JCLI-D-13-00274.1.

Colin de Verdière, A., 1988: Buoyancy driven planetary flow. *J. Mar. Res.*, **46**, 215–265, doi:10.1357/002224088785113667.

Collins, M., and B. Sinha, 2003: Predictability of decadal variations in the thermohaline circulation and climate. *Geophys. Res. Lett.*, **30**, 1306, doi:10.1029/2002GL016504.

——, and Coauthors, 2006: Interannual to decadal climate predictability in the North Atlantic: A multimodel-ensemble study. *J. Climate*, **19**, 1195–1203, doi:10.1175/JCLI3654.1.

Delworth, T. L., and M. E. Mann, 2000: Observed and simulated multidecadal variability in the Northern Hemisphere. *Climate Dyn.*, **16**, 661–676, doi:10.1007/s003820000075.

Dufresne, J.-L., and Coauthors, 2013: Climate change projections using the IPSL-CM5 Earth System Model: From CMIP3 to CMIP5. *Climate Dyn.*, **40**, 2123–2165, doi:10.1007/s00382-012-1636-1.

Epstein, E. S., 1988: Long-range weather prediction: Limits of predictability and beyond. *Wea. Forecasting*, **3**, 69–75, doi:10.1175/1520-0434(1988)003<0069:LRWPLO>2.0.CO;2.

Farrell, B. F., and P. J. Ioannou, 1996a: Generalized stability theory. Part I: Autonomous operators. *J. Atmos. Sci.*, **53**, 2025–2040, doi:10.1175/1520-0469(1996)053<2025:GSTPIA>2.0.CO;2.

——, and ——, 1996b: Generalized stability theory. Part II: Nonautonomous operators. *J. Atmos. Sci.*, **53**, 2041–2053, doi:10.1175/1520-0469(1996)053<2041:GSTPIN>2.0.CO;2.

——, and ——, 2001: Accurate low-dimensional approximation of the linear dynamics of fluid flow. *J. Atmos. Sci.*, **58**, 2771–2789, doi:10.1175/1520-0469(2001)058<2771:ALDAOT>2.0.CO;2.

Frederiksen, J. S., 2000: Singular vectors, finite-time normal modes, and error growth during blocking. *J. Atmos. Sci.*, **57**, 312–333, doi:10.1175/1520-0469(2000)057<0312:SVFTNM>2.0.CO;2.

Ganachaud, A., and C. Wunsch, 2000: Improved estimates of global ocean circulation, heat transport and mixing from hydrographic data. *Nature*, **408**, 453–457, doi:10.1038/35044048.

Gent, P. R., and J. C. McWilliams, 1990: Isopycnal mixing in ocean circulation models. *J. Phys. Oceanogr.*, **20**, 150–155, doi:10.1175/1520-0485(1990)020<0150:IMIOCM>2.0.CO;2.

Ghil, M., 2002: Natural climate variability. *Encyclopedia of Global Environmental Science*, Vol. 1, T. E. Munn, M. MacCracken, and J. Perry, Eds., J. Wiley and Sons, 544–549.

Goldenberg, S. B., C. W. Landsea, A. M. Mestas-Nuñez, and W. M. Gray, 2001: The recent increase in Atlantic hurricane activity: Causes and implications. *Nature*, **293**, 474–479, doi:10.1126/science.1060040.

Griffies, S. M., and K. Bryan, 1997: A predictability study of simulated North Atlantic multidecadal variability. *Climate Dyn.*, **13**, 459–487, doi:10.1007/s003820050177.

Hasselmann, K., 1976: Stochastic climate models: Part I. Theory. *Tellus*, **28A**, 473–485, doi:10.1111/j.2153-3490.1976.tb00696.x.

Hawkins, E., and R. Sutton, 2009a: Decadal predictability of the Atlantic Ocean in a coupled GCM: Forecast skill and optimal perturbations using linear inverse modeling. *J. Climate*, **22**, 3960–3978, doi:10.1175/2009JCLI2720.1.

——, and ——, 2009b: The potential to narrow uncertainty in regional climate predictions. *Bull. Amer. Meteor. Soc.*, **90**, 1095–1107, doi:10.1175/2009BAMS2607.1.

——, and ——, 2011: Estimating climatically relevant singular vectors for decadal predictions of the Atlantic Ocean. *J. Climate*, **24**, 109–123, doi:10.1175/2010JCLI3579.1.

Hirschi, J., J. Baehr, J. Marotzke, J. Stark, S. Cunningham, and J.-O. Beismann, 2003: A monitoring design for the Atlantic meridional overturning circulation. *Geophys. Res. Lett.*, **30**, 1413, doi:10.1029/2002GL016776.

Huck, T., and G. K. Vallis, 2001: Linear stability analysis of three-dimensional thermally-driven ocean circulation: Application to interdecadal oscillations. *Tellus*, **53A**, 526–545, doi:10.1111/j.1600-0870.2001.00526.x.

IPCC, 2013: *Climate Change 2013: The Physical Science Basis*. Cambridge University Press, 1535 pp.

Kushnir, Y., 1994: Interdecadal variations in North Atlantic sea surface temperature and associated atmospheric conditions. *J. Climate*, **7**, 141–157, doi:10.1175/1520-0442(1994)007<0141:IVINAS>2.0.CO;2.

Levitus, S., 1989: Interpentadal variability of temperature and salinity at intermediate depths of the North Atlantic Ocean, 1970–1974 versus 1955–1959. *J. Geophys. Res.*, **94**, 16 125–16 131, doi:10.1029/JC094iC11p16125.

Li, Y., S. Peng, and D. Liu, 2014: Adaptive observation in the South China Sea using CNOP approach based on a 3-D ocean circulation model and its adjoint model. *J. Geophys. Res. Oceans*, **119**, 8973–8986, doi:10.1002/2014JC010220.

Lorenz, E. N., 1963: Deterministic nonperiodic flow. *J. Atmos. Sci.*, **20**, 130–141, doi:10.1175/1520-0469(1963)020<0130:DNF>2.0.CO;2.

——, 1965: A study of the predictability of a 28-variable atmospheric model. *Tellus*, **17**, 321–333, doi:10.1111/j.2153-3490.1965.tb01424.x.

Madec, G., and M. Imbard, 1996: A global ocean mesh to overcome the North Pole singularity. *Climate Dyn.*, **12**, 381–388, doi:10.1007/BF00211684.

——, P. Delécluse, M. Imbard, and C. Lévy, 1998: OPA 8.1 ocean general circulation model reference manual. Institut Pierre-Simon Laplace Tech. Rep. 11, 91 pp.

Marti, O., and Coauthors, 2010: Key features of the IPSL ocean atmosphere model and its sensitivity to atmospheric resolution. *Climate Dyn.*, **34**, 1–26, doi:10.1007/s00382-009-0640-6.

Martinez-Villalobos, C., and D. J. Vimont, 2016: The role of the mean state in meridional mode structure and growth. *J. Climate*, **29**, 3907–3921, doi:10.1175/JCLI-D-15-0542.1.

Mignot, J., and S. Bony, 2013: Presentation and analysis of the IPSL and CNRM climate models used in CMIP5. *Climate Dyn.*, **40**, 2089, doi:10.1007/s00382-013-1720-1.

Msadek, R., K. W. Dixon, T. L. Delworth, and W. Hurlin, 2010: Assessing the predictability of the Atlantic meridional overturning circulation and associated fingerprints. *Geophys. Res. Lett.*, **37**, L19608, doi:10.1029/2010GL044517.

Mu, M., and Z. Zhang, 2006: Conditional nonlinear optimal perturbations of a two-dimensional quasigeostrophic model. *J. Atmos. Sci.*, **63**, 1587–1604, doi:10.1175/JAS3703.1.

Persechino, A., J. Mignot, D. Swingedouw, S. Labetoulle, and E. Guilyardi, 2013: Decadal predictability of the Atlantic meridional overturning circulation and climate in the IPSL-CM5A-LR model. *Climate Dyn.*, **40**, 2359–2380, doi:10.1007/s00382-012-1466-1.

Phillips, N. A., 1963: Geostrophic motions. *Rev. Geophys.*, **1**, 123–176, doi:10.1029/RG001i002p00123.

Pohlmann, H., M. Botzet, M. Latif, A. Roesch, M. Wild, and P. Tschuck, 2004: Estimating the decadal predictability of coupled AOGCM. *J. Climate*, **17**, 4463–4472, doi:10.1175/3209.1.

Redi, M. H., 1982: Oceanic isopycnal mixing by coordinate rotation. *J. Phys. Oceanogr.*, **12**, 1154–1158, doi:10.1175/1520-0485(1982)012<1154:OIMBCR>2.0.CO;2.

Salmon, R., 1998: *Lectures on Geophysical Fluid Dynamics*. Oxford University Press, 400 pp.

Sévellec, F., and A. V. Fedorov, 2013a: The leading, interdecadal eigenmode of the Atlantic meridional overturning circulation in a realistic ocean model. *J. Climate*, **26**, 2160–2183, doi:10.1175/JCLI-D-11-00023.1.

——, and ——, 2013b: Model bias reduction and the limits of oceanic decadal predictability: Importance of the deep ocean. *J. Climate*, **26**, 3688–3707, doi:10.1175/JCLI-D-12-00199.1.

——, and ——, 2015: Optimal excitation of AMOC decadal variability: Links to the subpolar ocean. *Prog. Oceanogr.*, **132**, 287–304, doi:10.1016/j.pocean.2014.02.006.

——, and T. Huck, 2015: Theoretical investigation of the Atlantic multidecadal oscillation. *J. Phys. Oceanogr.*, **45**, 2189–2208, doi:10.1175/JPO-D-14-0094.1.

——, and A. V. Fedorov, 2016: AMOC sensitivity to surface buoyancy fluxes: Stronger ocean meridional heat transport with a weaker volume transport? *Climate Dyn.*, **47**, 1497–1513, doi:10.1007/s00382-015-2915-4.

——, M. Ben Jelloul, and T. Huck, 2007: Optimal surface salinity perturbations influencing the thermohaline circulation. *J. Phys. Oceanogr.*, **37**, 2789–2808, doi:10.1175/2007JPO3680.1.

——, T. Huck, M. Ben Jelloul, N. Grima, J. Vialard, and A. Weaver, 2008: Optimal surface salinity perturbations of the meridional overturning and heat transport in a global ocean general circulation model. *J. Phys. Oceanogr.*, **38**, 2739–2754, doi:10.1175/2008JPO3875.1.

——, ——, ——, and J. Vialard, 2009: Nonnormal multidecadal response of the thermohaline circulation induced by optimal surface salinity perturbations. *J. Phys. Oceanogr.*, **39**, 852–872, doi:10.1175/2008JPO3998.1.

——, ——, and A. Colin de Verdière, 2010: From centennial to millennial oscillation of the thermohaline circulation. *J. Mar. Res.*, **68**, 723–742, doi:10.1357/002224011795977635.

Strogatz, S. H., 1994: *Nonlinear Dynamics and Chaos with Applications to Physics, Biology, Chemistry and Engineering.* Perseus, 498 pp.

Sutton, R. W., and D. L. R. Hodson, 2005: Atlantic Ocean forcing of North American and European summer climate. *Science*, **309**, 115–118, doi:10.1126/science.1109496.

Talley, L. D., J. L. Reid, and P. E. Robbins, 2003: Data-based meridional overturning streamfunctions for the global ocean. *J. Climate*, **16**, 3213–3226, doi:10.1175/1520-0442(2003)016<3213:DMOSFT>2.0.CO;2.

Taylor, K. E., R. J. Stouffer, and G. A. Meehl, 2012: An overview of CMIP5 and the experiment design. *Bull. Amer. Meteor. Soc.*, **93**, 485–498, doi:10.1175/BAMS-D-11-00094.1.

Teng, H., G. Branstator, and G. H. Meehl, 2011: Predictability of the Atlantic overturning circulation and associated surface patterns in two CCSM3 climate change ensemble experiments. *J. Climate*, **24**, 6054–6076, doi:10.1175/2011JCLI4207.1.

Tziperman, E., 1997: Inherently unstable climate behaviour due to weak thermohaline ocean circulation. *Nature*, **386**, 592–595, doi:10.1038/386592a0.

——, and P. J. Ioannou, 2002: Transient growth and optimal excitation of thermohaline variability. *J. Phys. Oceanogr.*, **32**, 3427–3435, doi:10.1175/1520-0485(2002)032<3427:TGAOEO>2.0.CO;2.

——, L. Zanna, and C. Penland, 2008: Nonnormal thermohaline circulation dynamics in a coupled ocean–atmosphere GCM. *J. Phys. Oceanogr.*, **38**, 588–604, doi:10.1175/2007JPO3769.1.

Vimont, D. J., 2010: Transient growth of thermodynamically coupled variations in the tropics under an equatorially symmetric mean state. *J. Climate*, **23**, 5771–5789, doi:10.1175/2010JCLI3532.1.

Weaver, A. T., J. Vialard, and D. L. T. Anderson, 2003: Three- and four-dimensional variational assimilation with a general circulation model of the tropical Pacific Ocean. Part I: Formulation, internal diagnostics and consistency checks. *Mon. Wea. Rev.*, **131**, 1360–1378, doi:10.1175/1520-0493(2003)131<1360:TAFVAW>2.0.CO;2.

Yoden, S., and M. Nomura, 1993: Finite-time Lyapunov stability analysis and its application to atmospheric predictability. *J. Atmos. Sci.*, **50**, 1531–1543, doi:10.1175/1520-0469(1993)050<1531:FTLSAA>2.0.CO;2.

Zanna, L., 2012: Forecast skill and predictability of observed Atlantic sea surface temperatures. *J. Climate*, **25**, 5047–5056, doi:10.1175/JCLI-D-11-00539.1.

——, and E. Tziperman, 2005: Nonnormal amplification of the thermohaline circulation. *J. Phys. Oceanogr.*, **35**, 1593–1605, doi:10.1175/JPO2777.1.

——, and ——, 2008: Optimal surface excitation of the thermohaline circulation. *J. Phys. Oceanogr.*, **38**, 1820–1830, doi:10.1175/2008JPO3752.1.

——, P. Heimbach, A. M. Moore, and E. Tziperman, 2011: Optimal excitation of interannual Atlantic meridional overturning circulation variability. *J. Climate*, **24**, 413–427, doi:10.1175/2010JCLI3610.1.

Zu, Z., M. Mu, and H. A. Dijkstra, 2013: Optimal nonlinear excitation of decadal variability of the North Atlantic thermohaline circulation. *Chin. J. Oceanol. Limnol.*, **31**, 1368–1374, doi:10.1007/s00343-014-3051-4.

——, ——, and ——, 2016: Optimal initial excitations of decadal modification of the Atlantic meridional overturning circulation under the prescribed heat and freshwater flux boundary conditions. *J. Phys. Oceanogr.*, **46**, 2029–2047, doi:10.1175/JPO-D-15-0100.1.